

Grapenthin Ronni (Orcid ID: 0000-0002-4926-2162)

Person Mark, Austin (Orcid ID: 0000-0003-0503-1845)

Folsom Matthew (Orcid ID: 0000-0002-9079-6684)

Decadal-scale aquifer dynamics and structural complexities at a municipal wellfield revealed by 25 years of InSAR and recent groundwater temperature observations

Ronni Grapenthin^{1,2}, Shari Kelley³, Mark Person¹, and Matthew Folsom¹

¹ New Mexico Institute of Mining and Technology, Department of Earth & Environmental Sciences, New Mexico Tech, 801 Leroy Place, Socorro NM 87801

² Now at: University of Alaska Fairbanks, Geophysical Institute, 2156 Koyukuk Drive, Fairbanks, AK 99775

³ New Mexico Bureau of Geology and Mineral Resources, New Mexico Tech, 801 Leroy Place, Socorro NM 87801

For submission to Water Resources Research

September 10, 2019

This article has been accepted for publication and undergone full peer review but has not been through the copyediting, typesetting, pagination and proofreading process which may lead to differences between this version and the Version of Record. Please cite this article as doi: 10.1029/2018WR022552

Abstract

Over the past 35 years the Buckman wellfield near Santa Fe, New Mexico, experienced production well drawdowns in excess of 180 m, resulting in ground subsidence and surface cracks. Increased reliance on surface water diversions since 2011 has reduced pumping and yielded water level recovery. To characterize the impact of wellfield management decisions on the aquifer system, we reconstruct the surface deformation history through ERS, ALOS, and Sentinel-1 InSAR time series analysis during episodes of drawdown (1993-2000), recovery (2007-2010) and modern management (2015-2018) in discontinuous observations over a 25-year period. The observed deformation generally reflects changes in hydraulic head. However, at times during the wellfield recovery, the deformation signal is complex, with patterns of uplift and subsidence suggesting a compartmentalized aquifer system. Recent records of locally high geothermal gradients and an overall warming of the system ($\sim 0.5^{\circ}\text{C}$ during the water level recovery) obtained from repeat temperature measurements between 2013 and 2018 constrain a conceptual model of convective heat transfer that requires a vertical permeable zone near an observed fault. To reproduce observed temperature patterns at monitoring wells, high basal heat flow and convective cooling associated with downward flow of water from cool shallow aquifers during the drawdown period is necessary. The fault, however, appears to die out southward or may be locally permeable, as conceptual cross-sectional hydrologic modeling reproduces the surface deformation without such structure. Our work demonstrates the importance of incorporating well-constrained stratigraphy and structure when modeling near-surface deformation induced by, for instance, groundwater production.

(250/250 Words)

Short Title: Decadal-scale aquifer dynamics from InSAR, Temperatures and Modeling

Key Points:

1. InSAR spanning 25 years reveals complex surface deformation dynamics due to groundwater production and suggests permanent storage loss
2. Locally high geothermal gradients and groundwater warming suggest groundwater upflow through a mapped, vertically permeable fault
3. Conceptual cross-sectional hydrologic modeling informed by InSAR suggests a discontinuous or locally permeable fault/stratigraphic discontinuity

1 Introduction

Several recent hydrological studies have used water level data and Interferometric Synthetic Aperture Radar (InSAR) to monitor aquifer depletion, recovery and dynamics [Amelung et al., 1999; Bawden et al., 2001; Bell et al., 2002; Hoffmann et al., 2001, 2003a; Reeves et al., 2011; 2014; Chaussard et al., 2014, 2017, Chen et al., 2016; Miller et al., 2017; Murray and Lohmann, 2018]. Collectively, these studies keep demonstrating the utility of InSAR data products and highlight a viable method for resource monitoring by water managers in arid regions. While general spatio-temporal trends of aquifer production and recharge in a pattern recognition sense can be insightful [e.g., Murray and Lohman, 2018], a goal of such analyses should be to quantify subsurface processes and properties, and retrieve these from the data. Progress has been made to infer properties such as elastic skeletal storage on basin scale through combination of InSAR and well data, and retrieve water level changes without well measurements with respectable accuracy [e.g., Chaussard et al., 2014, Chen et al., 2016]. However, on smaller scales, linking surface displacements to hydro-dynamic processes in the shallow subsurface, such as pumping-induced head changes or aquifer recharge, can be significantly impacted by small scale geologic features such as permeable sand channels or faults, and lateral variations in stratigraphy in general.

Collection of thermal profile data, which involves measuring subsurface temperature as a function of depth, can be used to measure groundwater flow [Anderson, 2005; Saar, 2011; Kurylyk et al. 2018]. The shape of a thermal profile can help to identify and quantify downflow (concave-up); upflow (convex-up), or lateral flow (abrupt cooling or warming associated with a certain aquifer). Few hydrologic studies have examined the impact of aquifer depletion and recovery on subsurface temperatures. Taniguchi [1995] used discharge temperatures collected from an actively-pumping wellfield in the Nara basin in Japan to document aquifer cooling between 1963 and 1993. He noted that the temperature in one well decreased by 2.35°C and attributed this cooling to an increase in the rate of

groundwater flow caused by a decreasing hydraulic head, thus reducing the thermal energy picked up by the groundwater during flow.

Here we combine these two very different approaches of monitoring changes in groundwater flow using satellite radar and well temperature observations, and highlight complications that small scale structure and stratigraphy can add to interpretations.

Temperature measurements as a function of depth in monitoring wells can be utilized to infer groundwater movement and aquifer compartmentalization. We find that temperature observations constraining local geothermal gradients provide essential information on small-scale stratigraphy and structure required to establish a meaningful conceptual framework for modeling surface deformation due to the depletion and recovery of a municipal wellfield operating in an arid setting. Repeat thermal profile measurements locally confirm vertical groundwater flow that InSAR observations broadly suggest, meaning that remote observations could become not just a proxy for mass flux, but also temperature change.

We first reconstruct 25 years (1993-2018) of surface ground deformation for the municipal Buckman wellfield (BWF) near Santa Fe, New Mexico, USA, from episodic InSAR analysis utilizing the ERS (European Remote Sensing Satellites, e.g., Attema 1991), ALOS (Advanced Land Observing Satellite, e.g., Shimada et al., 2010), and Sentinel-1 (e.g., Torres et al., 2012) synthetic aperture radar (SAR) satellite platforms. Next, we present repeat thermal profile data from monitoring wells in the field. Groundwater temperature time series, rarely reported for high-production wellfields, from 2013-2018 exhibit warming trends due to flow, recharge and surface warming. Following this, we explain the temperature observations with one-dimensional conductive-convective heat transfer modeling. These inform the realistic geology that is incorporated into a conceptual two-dimensional hydrogeologic model of pumping-induced surface displacements driven by production well water-level observations to qualitatively reproduce the InSAR observations. We generally approximate first-order surface displacement characteristics observed from the satellite platforms when the displacement is driven by pumping records alone. Our work shows the complexities

involved when interpreting surface displacements induced by shallow subsurface dynamics and lateral variations in stratigraphy and structure.

2 Background

2.1 Geologic History and Regional Hydrology

The BWF is in the hydrologic discharge zone of the Española Basin, a westward-dipping half-graben located in the Rio Grande rift [Koning and Read, 2010; Figure 1]. The basin is situated between the Proterozoic-cored Sangre de Cristo Mountains to the east, which is a Laramide uplift feature, and the Miocene to Pleistocene Jemez Mountains volcanic field to the west. The Rio Grande flows along the axis of the basin, a few hundred meters west of the edge of the field. The BWF is developed in arkosic sandstones, siltstone, and conglomerate of the Chamita Formation within the Santa Fe Group. The Chamita Formation was deposited by a south-flowing ancestral Rio Grande; the sandy, axial-river deposits interfinger with alluvial slope deposits derived from the west and fine-grained basin floor facies derived from the east [Koning et al., 2007; Koning and Read, 2010]. Thus, the wellfield taps highly productive, but laterally discontinuous, fluvial aquifers. Geophysical models constructed by Grauch et al. [2009] show the base of the Santa Fe Group is less than 600 m below land surface (bls) near the Sangre de Cristo range front to the east, and deepens to nearly 2700 m bls at the BWF. Aquifers beneath the Pajarito Plateau that are recharged in the Jemez Mountains dip to the west, away from the wells at Buckman, and thus do not provide recharge to the BWF. Los Alamos National Laboratory, located on the Pajarito Plateau on the flanks of the Jemez Mountains to the west of the BWF, conducts extensive groundwater sampling at piezometer nests (SF2B, 3, and 4; Figure 1) in the BWF to detect laboratory-derived contaminants and to this date, no contaminants have been detected [LANL, 2012].

The BWF production wells (Figure 1) penetrate the confined Chamita aquifer system, with depths of the production wells ranging from 277 m (B8) to 486 m (B2) bls in the northwestern portion of the field; in the southeastern portion of the field, the wells are

completed as deep as 610 m bls (B13). The shallowest upper screen in any production well is 71 m bls (B2). Screened intervals in piezometers that sample water-bearing sand lenses deeper than 50 m in the northwestern portion of the field show no connection between water levels and river stages, further reinforcing the conclusion of a confined aquifer system [Vesselinov et al., 2014].

Groundwater flow in the Buckman region is characterized by low horizontal hydraulic gradients and high vertical hydraulic gradients [McAda and Wasiolek, 1988; Johnson et al., 2013]. McAda and Wasiolek [1988] developed a regional-scale hydrologic model for the Santa Fe Group aquifer of the Española Basin that was calibrated using pre-development hydraulic head and hydrologic data. This model matched the pronounced vertical hydraulic head gradient and discharge measured near the Rio Grande. Upward groundwater flow near the river is supported by upward-directed hydraulic gradients (0.03-0.13) observed in piezometer nests, elevated groundwater temperatures, and elevated concentrations of conservative ions (boron, lithium) [McAda and Wasiolek, 1988; Johnson et al., 2013]. However, production activities have locally altered the pre-development gradients.

Fluctuations in groundwater temperature have been observed in recorded discharge temperatures of the BWF production wells. Kelley et al. [2016] noted that summer discharge temperatures have been gradually rising since 2008 and that B1 appears to draw in cooler waters during times of high withdrawals. Discharge temperatures in B8, the well that is closest to a mapped fault (B8F in Figure 1), are consistently warmer than the other production wells by 2 – 3 °C.

2.2 History of the Buckman Wellfield

The BWF is one of five sources that supply drinking water to city of Santa Fe [Annual Water Report, 2018]. Early in the wellfield's history the BWF provided 50% of the city's water, but during the last five years its contribution has shrunk to <10%. Initially six wells were drilled in the northwestern part of the field near the Rio Grande in 1971 and 1972. Wells B1 and B2 were replaced in 1977 and well B3 was replaced in 1995. The U.S.

Geological Survey drilled monitoring well nests SF2B, SF3, and SF4 for the City of Santa Fe in 1986 and 1987. Two additional production wells in the northwestern field, wells B7 and B8, were drilled in 1990 (Figure 1). The field produced an average of 544 ± 122 million liters/month between 1993 and 2003 [Shomacker and Associates, 2018], which resulted in water level declines of 100 to 200 m during this time [Figures 2, S1-2; LANL, 2012; Shomacker and Associates, 2018]. This precipitous drop in water levels induced ground subsidence up to about 20 mm/yr or a maximum of 14 cm over a 25 km² area from 1993 to 2000 observed with InSAR [Thomsen and Fialko, 2004; our Section 3 and Figures 3, S1-3]. In 2001, to the east of this portion of the field, a fissure about 800 m long with 20 cm of dilation and 20-25 cm of down-to-the-west vertical offset formed parallel to the pattern of subsidence along the East Buckman fault (EBF; Figure 1) [Koning et al., 2007; Haneberg, 2010]. Such fissures have been observed in other basins experiencing inelastic compaction [e.g., Galloway et al. 1998; Pavelko, 2004].

The wellfield expanded toward the southeast in 2002 and 2003 when production wells B9-B13 were brought on-line in an effort to reduce overpumping in the older part of the BWF. Production in the main part of the field dropped to 266 ± 108 million liters/month between 2004 and 2011 and the remaining production shifted to the southeast (wells B10 – B13, Figures 1 and 2), which stabilized water levels in the original field after an average drop between 120 – 170 m [Shomaker and Associates, 2014]. In 2012, the City of Santa Fe completed the Buckman Direct Diversion project (BDD), diverting additional water from the Rio Grande as part of the San Juan-Chama Project [BDDproject.org]. The city currently forecasts that no additional resources are required until 2020. This history is best visualized as three distinct periods of groundwater use (Figure 2A). Water levels at B1, B4, B6 and B8 are shown for comparison (Figure 2B); detailed depth-to-water plots for all the wells can be found in Shomacker and Associates [2018] and at https://www.santafenm.gov/buckman_wells_water_level_monitoring_program.

3 InSAR Analysis

3.1 Data and Image Processing Methods

We performed InSAR analysis on data from the ERS (European Space Agency, ESA), ALOS (Japanese Aerospace Exploration Agency, JAXA), and Sentinel-1 (ESA) missions. Details on analyzed tracks, frames, number of scenes and respective time periods are given in Table 1. Table 1 also lists the master image we picked for each sensor to align the remaining scenes for time series analysis with GMTSAR [Sandwell et al., 2011a,b] using SRTM-3 [Farr et al., 2007] digital elevation models for terrain corrections.

After an initial run we eliminate pairs with poor correlation and heavily affected by atmosphere (e.g., water vapor or ionospheric activity). Correlation between two SAR images is calculated on a pixel scale, and provides a quality metric for any given location. We generally benefit from longer-term temporal coherence due to minimal vegetation [e.g., Wei and Sandwell, 2010] in the region of the BWF, but still had to eliminate highly de-correlated data below a pixel-based correlation threshold of 0.12. We unwrapped the remaining phase observations for the region of interest shown in Figures 3-5 with *snaphu*, an algorithm that turns modulo 2π radian phase observations of interferograms (fringes) into unambiguous phase [Chen and Zebker, 2000], and stacked the unwrapped interferograms for each sensor to determine average line-of-sight (LOS) velocities for the respective time periods. LOS velocities are surface motions projected onto the view angle of a stable satellite. LOS lengthening, i.e., a longer distance between satellite and an object on the ground, can be induced by subsidence, horizontal motion away from the satellite, or a combination of both. LOS shortening, in turn, is induced by the opposite ground motion.

The earlier periods observed with ERS and ALOS have fewer high quality observations, therefore we abstained from higher-resolution time series analysis [e.g., SBAS, Berardino et al., 2002]. We removed constant biases in each velocity field by averaging over a representative region with zero expected surface deformation and minimal topographic effects (indicated by red lines along profiles in Figures 3-5). This process is

somewhat subjective and may bias the results by a constant that is reported in the last column of Table 1 for each velocity product.

Significant noise sources in InSAR data are due to variations in the ionosphere, variations in tropospheric water content, and imperfect digital elevation models or topographically driven tropospheric changes between SAR acquisitions that remain unmodeled. Topography in mountainous areas locally influences air temperature and moisture content, and as a result creates tropospheric delays that may mimic topography [Delacourt et al., 1998]. While the region of the wellfield has minimal topography and relatively higher correlation values, we find significant topography outside of the valley (Figure 1) generally causing slight atmospheric effects (Figures 3-5). In general, we base our averaged LOS velocity calculations on interferograms with minimal impact of such effects.

3.2 InSAR Results

We obtain results for three disconnected time periods determined by availability of data from the utilized SAR platforms (Figure 2B): 1993-2000 (ERS; Figure 3), 2007-2010 (ALOS; Figure 4), and 2015-2018 (Sentinel-1, Figure 5) during which we observe significant changes in the long-term deformation field driven by wellfield management and climate impacts. Since matrix compaction and expansion in the shallow subsurface drive the deformation processes, we assume that the observations reflect predominantly (not exclusively, see e.g., Fuhrmann and Garthwaite, 2019) vertical motions. This is confirmed by a comparison of average LOS velocities from two different viewing geometries (ascending and descending ERS for the 1993-2000 time frame) showing similar features and sense of motion for the BWF (Figure S3). Even if elastic flexure due to surface loading and unloading was invoked, the deformation would manifest predominantly in the vertical component [e.g., Grapenthin et al., 2006; Pinel et al., 2007].

The observations from 1993-2000 (Figure 3) indicate broad subsidence over the entire northwestern wellfield at a maximum of about 20 mm/yr LOS lengthening (ERS: 23° look angle) with maximum deformation in its center near well B2 (Figures 1,3). During this

time period only wells B1-8 were active, hence, we do not expect any deformation outside of the core wellfield. The N-S and E-W profiles through the center of deformation show that the subsidence is indeed focused on the wellfield with little to no marginal uplift, which could be expected due to elastic flexure after unloading [e.g., Amos et al., 2014; Borsa et al., 2014], but likely requires significantly larger mass removal to manifest above the observed noise floor. Some relative LOS shortening (e.g., uplift) in the NW quadrant and east of the wellfield in Figure 3 correlates with higher topography and is interpreted as atmospheric interference.

Between 2007 and 2010 (Figure 4, ALOS: 34° look angle), we observe an intriguing pattern of about 20 mm/yr of average LOS-shortening (approx. uplift) in the western part of the wellfield and up to 10 mm/yr of average LOS-lengthening (approx. subsidence) in the eastern part. Most, if not all, of the uplift occurs near well B8 (Figure 4), where water levels recovered by ~60 m from 2009 to 2010, approaching pre-development levels (Figure 2). Wells B1 and B7, also in the vicinity of this signal, recovered by ~100 m (B1) from 2007-2010 (Figure 2), but do not show as dramatic an uplift signal, which is potentially eclipsed by the subsidence in the southeastern part of the wellfield that is centered on wells B3-5 (Figure 4). The opposing motion is in agreement with the general trend of well water levels during the observation period (Supplemental Figures S1,S2). The sharp discontinuity between these regions with opposite polarity in motion approximately corresponds with the location of a north-trending, normal fault, dipping to the east and mapped by Koning and Read [2010] (B8F in Figure 1). These patterns are suggestive of aquifer compartmentalization consistent with a conduit/barrier fault [Bense and Person, 2006].

We split the observations from 2015-2018 into two time intervals (Figure 5). The almost complete lack of snow pack in all of New Mexico and southern Colorado during the winter 2017/2018 (e.g., National Weather Service, 2018) and the resulting lack of surface water supply increased the demand for groundwater, which warrants separate consideration of observations for 2018 (Figure 5B). The earlier time period from 2015-2017 (Figure 5A) shows slight and very narrow LOS lengthening with a maximum of about 13-17 mm/yr at well

B1. While the well water levels at B1 and B8 (Figure 2B) show slight recovery compared to the not-imaged period from 2011-2015, the monitoring wells in the vicinity (SF3A, SF4A) show a significant, albeit short-lived, lowering of well water levels toward the end of 2017 (Figure 2C). The resulting short-term, but large amplitude signal in the observed ground deformation biases the long-term displacement field toward subsidence. Importantly, however, we find this LOS lengthening to be of very short wavelength, before overall stable background motion with slight LOS shortening to the west and north in regions away from topography. This is particularly evident in the EW profile where we see a sharp drop in LOS velocity within a subtle, but broad LOS increase in the region of prior subsidence near well B8.

This picture changes dramatically in 2018 (imaged through end of October, Figure 5B) where we see the eastern part of the wellfield (wells B3-6, B9) induce significant LOS lengthening of up to 50 mm/yr due to increases in production (particularly well B4) in response to the lack of surface water flows or otherwise driven drops in water levels (Figures 2B, 5B). Again, the velocity drops sharply as we move from west to east across the profile and recovers somewhat more gently at the eastern edge of the wellfield. The shorter imaged time interval results in larger background noise, again well correlated with topography. A feature of note outside of the primary study region is the subsidence imaged south of Cuyamungue in the NE of Figure 5B. This LOS lengthening on the order of 30 mm/yr is likely also caused by increased production from local wells.

4 Groundwater Temperature Fluctuations

The primary goal of measuring temperature as a function of depth (thermal profiles) in the monitoring wells in the Buckman area is to map out groundwater movement and compartmentalization in the complex fluvial aquifer system beneath the municipal wellfield. In addition, repeat measurements were collected annually in mid-summer from 2013–2018 to determine temporal variations in temperature caused by rising water levels (Figure 2C) and mean annual air temperatures (Figure 2D) during this timeframe. This timing coincided

with the installation of the Buckman Direct Diversion and diversions from the older portion of the BWF were at their lowest levels in two decades (Figure 2A). Here we focus on thermal profiles measured in monitoring well nests SF4, SF3 and SF2 (Figures 1, 6, 7, and 8). Each nest has three wells (A,B,C) of decreasing depth. Each well has a short, 3-m screened interval, located at or near the bottom of the casing. The deepest monitoring well in the field, SF2A, was damaged in 1999 during the peak of subsidence and is no longer accessible.

4.1 Methods

Students attending the Summer of Applied Geophysical Experience (SAGE) program recorded thermal profiles in monitoring well nests located in the BWF and elsewhere in the Española Basin during the summers of 2013-2018. Temperature logging equipment used by SAGE consists of a Fenwall thermistor attached to a wireline cable that is mounted in a pickup truck covered with a camper shell. A digital multimeter attached to a computer records resistance in the thermistor, which is converted to temperature by calibrating the truck-based system against a laboratory-calibrated platinum resistance thermometer. This calibration is done once a year, and through the years of the experiment (2013-2018), the annual calibration points lie on the calibration curve that was established using five years of data. In other words, the calibration of the thermistor did not change during the experiment. Measurements in the field are taken at 1 m intervals, and the cable is lowered down the well at a rate of 2 m/minute. Repeat measurements in regional wells outside the area of aquifer development are reproducible year-after-year to ± 0.02 °C using this equipment. One source of error is associated with difficulties in starting the thermistor at the same elevation relative to the ground surface during each repeat measurement; this error is less than 0.5 m. Vertical geothermal gradients, dT/dz , are estimated by linear regression using least squares estimation.

4.2 Spatial Variations in Well Observations Constrain Stratigraphy

The geothermal gradients in the monitoring wells vary significantly over short horizontal distances (Figures 6, 7). Monitoring wells SF3A, SF4A and SF2C are screened in

the same depth interval and have been interpreted by some as sampling the same aquifer [LANL, 2012; Vesselinov et al., 2014]. However, geothermal gradients range from 79.6 and 73.1 °C/km in SF4A and SF3A, respectively, to 38.0 °C/km in SF2C over a horizontal distance of only 300 m (Figures 6, 7). Above 100 m, the temperatures in SF2B follow those in SF2C exactly (Figures 6,8), then at greater depths, the geothermal gradient increases, likely due to changes in rock type determined on the resistivity log of SF2A, located 3 m south of SF2B [Hart, 1989]. The best-fit linear gradients for SF2B are 38.0 °C/km above 120 m and 57 °C/km between 120 and 160 m (Figure 8), still well below the calculated gradients in SF3A and SF4A. Mapped faults have not been identified between the SF2 and SF3 nests [Koning and Read, 2010]. Analysis of drillers and geophysical well logs indicates that the sand and clay intervals between these wells are discontinuous (Figure 7). A comparison of published geochemistry data [Johnson et al., 2013; LANL, 2012] reveals that there are also changes in both major ions and trace elements between wells SF3A and SF2C, but not between SF3A and SF4A, indicating that the SF3A/SF4A pair and SF2C are screened in different sand lenses (Figure 7). The abrupt change in geothermal gradient and water chemistry suggests a stratigraphic discontinuity in the aquifers between SF2 and SF3. In contrast, the elevated geothermal gradients in SF3 and SF4 appear to be related to slightly warm water migrating up a small fault mapped by Koning et al. [2007] (Figure 1, B8F). SF4 is closer to the fault and has the higher geothermal gradient.

4.3 Temporal Groundwater Temperature Fluctuations

Generally, thermal profiles measured in SF3 and SF4 between 2013 and 2018 generally show warming by ~0.3–0.4°C between 2014 and 2018, with the largest change occurring in 2015 (Figure 6). In detail, repeat measurements at SF3 and SF4 between 2013 and 2014 showed little change; the geothermal gradients were generally linear. Upon arrival at the wells in 2015, we found that SF3A and SF4A had been capped by the USGS because of artesian flow to the surface, which precluded measurement of these wells in that year. Instead, we logged SF3B and SF4B, which had water standing in the casing ~0.5 m above

the ground surface. Temperatures in SF3B had never been measured before, and SF4B was measured in 2013. The temperature in SF4B shifted 0.2°C through the length of the 40 m hole between 2013 and 2015. The 2016 measurements showed a continued warming trend in the SF3 and SF4 nests. Water levels had dropped since 2015 and we obtained temperature measurements in all four deeper wells in the SF3 and SF4 nests. Remarkably, the temperature in SF4A had warmed 0.3 °C along the 80 m length of the borehole. In contrast, the temperatures near the bottom of the shallow wells SF3B and SF4B remained similar compared to 2015, but the upper parts of these wells warmed. SF4B shows the largest increases in temperature (close to 0.5 °C) between 10 and 30 m depth. Similarly, the bottom of deep well SF3A remained at temperatures like those measured in 2014, and the top part of this well also warmed. Temperatures continued to rise in 2016 and 2017. In summary, temperatures at the bottom of SF3 and 4 have increased by 0.28–0.37°C (± 0.02 °C) between 2014 and 2018, with the most dramatic change occurring between 2014 and 2016. Artesian flow in SF3A/B and SF4A/B began in 2015 and water levels have risen 2.5–8 m over the period of observation. The upward flow of water in the wellbores has caused the upper parts of the wells to warm by as much as 0.8–1.3°C since 2014.

Temperatures were logged in SF2B every year between 2013 and 2018 and this well was also logged by Manning [2009] in 2005 (Figure 8). SF2C was also logged multiple times during this timeframe (Figure 6). SF2C is on average 0.1 °C warmer in 2016 and 2017 compared to 2013. This small difference is within the precision of the thermistor and the elevation of the thermistor when logging begins. In contrast, the thermal profiles for the deeper parts SF2B have changed significantly over the years. In general, the temperature log for SF2B was reproducible to within 0.1 °C between 2013 and 2015, except in the depth range between 205 - 230 m which corresponds to a sandy zone within an interval dominated by silt; the base of this depth range is located ~15 m above the screened interval near the bottom of the well (screen at 244-247 m). Initially, especially visible in the Manning [2009] log, this interval was relatively cool compared to the background gradient and the interval

warmed between 2013 and 2015. Then in 2016 and 2017, and to a lesser degree, in 2018, temperatures below 125 m started to oscillate above and below the curves measured in previous years. A region of slightly warmer temperatures developed near the top of the interval that was cool in 2005, so the water flowing around the casing appears to be warming. We attribute this unusual behavior to possible damage of the casing, which is allowing water to enter, thus causing convection within the wellbore. Examination of the casing with a camera will be necessary to confirm this.

5 Modeling

5.1 One-Dimensional Conductive-Convective Heat Transfer

In order to understand the temperature patterns within monitoring well SF3A, we constructed a suite of idealized one-dimensional models of groundwater flow and heat transfer in order to calculate temperature profiles in the well. We solved the following groundwater flow equation in one dimension:

$$S_s \frac{\partial h}{\partial t} = \frac{\partial}{\partial z} \left[K_z \frac{\partial h}{\partial z} \right] \quad (1)$$

where S_s is specific storage, K_z is the vertical hydraulic conductivity, h is hydraulic head, t is time and z is elevation. We used a model domain that was about 500 m deep and an element spacing of 2 m. We imposed drawdowns from well B1 between 1982 and 2016, which include periods of drawdown (1982-2000) and recovery (2000-2016). Specified hydrostatic head boundary conditions were set on the top and bottom of the 500-m-thick solution domain based on well observations (Figure 9). We assumed a hydrostatic head initial condition and upper boundary condition of 1683 m. This elevation represents the topographic low of the model cross section. Vertical groundwater velocities were calculated using Darcy's law:

$$q_z = -K_z \frac{\partial h}{\partial z} \quad (2)$$

where q_z is the vertical Darcy flux. We then solved the following transient conductive-convection heat transfer equation [Bredehoeft and Papodopolus, 1965]:

$$C_b \frac{\partial h}{\partial t} = \frac{\partial}{\partial z} \left[\lambda_b \frac{\partial T}{\partial z} \right] - q_z \rho_f C_f \frac{\partial T}{\partial z} \quad (3)$$

where T is temperature, C_b is the bulk heat capacity (solids plus fluids), λ_b is the bulk thermal conductivity (solids plus fluids), C_f is the fluid heat capacity, and ρ_f is the fluid density. We varied the specified heat flux boundary between 80 and 170 mW/m² at the base of the solution domain. We imposed a linear temperature gradient with depth as an initial condition consistent with the basal heat flux. Mean annual changes in land surface temperature based on measurements at the Santa Fe airport were imposed at the top of the model domain (Figure 9). These data showed a warming trend with significant variability.

5.2 Hydrothermal Model Results

We assessed the effects of permeability and changes in the upper specified temperature boundary conditions on simulated temperatures using our idealized one-dimensional hydrothermal model to observed temperature profiles from 2013 to 2016 in well SF3A (Figure 10). Our primary goal in developing these models was to understand whether the curvature in the temperature profiles between depths of 20–60 m in well SF3A could be explained by convective heat transfer effects combined with changes in temperatures at the water table. We hypothesize that these changes are due to climate change and convective cooling effects during times of high production in the wellfield (see Figure 2D).

We used a bulk specific storage within the upper 500 m of 4.0×10^{-6} /m similar to that specified in the cross sectional hydrogeologic model described in the next section. We assigned a thermal conductivity of 1.93 W/m-K assuming a porosity of 0.3 and a thermal conductivity of the solids of 2.5 W/m-K for all units below the water table. We used the drawdown history to adjust the thermal conductivity of the shallowest vadose zone elements to 1.72 W/m-K for air-saturated pores. This had a second order effect on simulated temperatures. We varied the bulk permeability of the 500 m thick column from 10^{-16} to 10^{-14}

m². These values fall approximately in between the permeability of the aquifers and confining units for an intermediate permeability scenario (10⁻¹⁶ to 10⁻¹¹ m²). We also varied the basal heat flux between 80 to 200 mW/m². We found best fits to the observed temperature profile with a bulk permeability of 10^{-15.1} m² for the model domain and a basal heat flux of 170 mW/m² (Figure 10B,D). Typical values of basal heat flow for the Rio Grande Rift do not exceed 80 mW/m² (Reiter et al., 1975), but using this value produces much lower deep thermal gradients than are observed (compare Figure 10B to 10E).. This corresponds to a thermal Peclet number of 1.6. The one-dimensional Peclet number is given by:

$$Pe = \frac{HC_f \rho_f q_z}{\lambda_b} \quad (4)$$

where Pe is the thermal Peclet Number (ratio of convective to conductive heat transport) and H is domain length. Best-fit models involved assigning permeability conditions that allowed for downward convective cooling, simulating the influx of cool water from shallow aquifers during times of drawdown (compare Figures 10A-C). Increasing the permeability to 10^{-14.8} m² resulted in too much curvature in the simulated temperature profile (Figure 10C). Reducing the permeability to 10⁻¹⁶ m² resulted in more conductive temperature profiles ($Pe=0.2$) with the only variations in simulated temperatures being due to the imposed mean annual air temperature at the top of the model domain (Figure 10A). Large changes in water table temperatures were realized by using the mean annual air temperature as the top specified value boundary conditions in the heat transfer model (Figure 10D). However, the observed change in water table temperatures in well SF3A did not monotonically increase 2013 – 2016. These simple hydrothermal models were unable to reproduce the observed offsets in the temperature profiles in the depth range from 20-60 m between 2013-2016 observed in the data.

5.3 Conceptual Cross-Sectional Models of Pumping, Subsidence, and Uplift

Informed by the temperature observations and thermal modeling, we developed a suite of idealized cross-sectional models in order to assess how changes in simulated hydraulic head would affect land subsidence/uplift in response to pumping. One important goal of these conceptual hydrologic models is to try to understand how the presence of fault zone B8F (Figure 1) between the B4 and B8 production wells could account for the observed differential west to east uplift/subsidence across the Buckman wellfield between 2007 and 2010 (Figure 4). These two wells were used because they are located in the respective centers of the bimodal deformation field in Figure 4, had representative pumping/drawdown histories and were located on either side of the fault zone shown in Figure 7. We hypothesize that the presence of the fault zone may have played an important role in modifying temporal uplift/subsidence patterns adjacent to the B4 and B8 production wells. A second goal of these models is to assess whether or not the inferred subsidence rates and their spatial characteristics across the Buckman wellfield observed with InSAR could be reproduced using an elastic/inelastic hydromechanical model [Hoffman et al. 2003b].

The governing groundwater flow equation we solved in this study is given by:

$$S_s \frac{\partial h}{\partial t} = \frac{\partial}{\partial x} \left[K_x \frac{\partial h}{\partial x} \right] + \frac{\partial}{\partial z} \left[K_z \frac{\partial h}{\partial z} \right] \quad (5)$$

where S_s is specific storage (m^{-1}), h is hydraulic head (m), K_x and K_z ($m \text{ s}^{-1}$) are the components of hydraulic conductivity in the x- and z-directions. Hydraulic conductivity in m/s is related to permeability as follows: $K_x = \frac{k_x \rho_f g}{\mu}$ where k_x is permeability in the x-direction, ρ_f is fluid density, g is the gravity constant, and μ is fluid viscosity. Specific storage was varied depending on whether the vertical effective stress (σ_e) exceeded the pre-consolidation stress (σ_z^{max}) as described by Hoffman et al. (2003b):

$$S_s = S_{ske} \quad \sigma_z^{max} < \sigma_z \quad (6a)$$

$$S_s = S_{skv} \quad \sigma_z^{max} \geq \sigma_z \quad (6b)$$

where S_{ske} is the elastic, skeletal specific storage coefficient, S_{skv} is the inelastic or virgin storage coefficient, σ_e is the vertical effective stress ($\sigma_e = \sigma_v - P$), σ_v is the vertical load and P is fluid pressure. We did not vary the value of S_s based on lithology. We made this assumption, in part, because the coarse-grained facies are heterogeneous containing silt and clay stringers, and because laboratory compressibility data for these sediments were not available to us. Since land surface erosion and sedimentation can be neglected on these time scales, we assumed that $\Delta\sigma_z = \Delta h \rho_f g$. The preconsolidation effective stress is exceeded when simulated heads are less than the preconsolidation (hydrostatic) heads. According to Hoffman et al. [2003b] S_{skv} (inelastic deformation) should be much greater than S_{ske} (elastic deformation). In addition, S_{ske} is typically assumed to be a non-linear function of effective stress change during inelastic deformation. In this study, we did not vary S_{skv} incrementally with changes in effective stress during inelastic deformation. We set S_{skv} about 1.5 greater than S_{ske} . As noted in Hoffman et al. [2003b], the use of “two constant values for the skeletal specific storage, one each for stresses greater than and less than the preconsolidation stress, only approximates the true stress/compaction relation of the sediments.” Laboratory compressibility-effective stress data for the Buckman wellfield were not available to evaluate either S_{skv} or S_{ske} .

Because we used a cross sectional model in this study, we did not include a pumping well sink term in our governing groundwater flow equation. Rather, the head changes observed in the B4 and B8 wells were imposed in all model runs along the well screen intervals (Figures 2B, S1, S2). We specified hydrostatic hydraulic heads along the top of the model domain and no-flux boundaries along all other sides. We did not attempt to represent the pre-pumping regional flow field in these models. We assumed a hydrostatic initial condition prior

to the onset of pumping. We calculated land subsidence using a linear elastic/inelastic formulation described by Hoffman et al. [2003b]:

$$L_i(t) = \sum_i S_s \Delta h_i(t) \Delta b_i; \quad (7)$$

where $L_i(t)$ is the change in land surface elevation for a given nodal column (see below), Δb_i is the vertical width of the i^{th} element, and $\Delta h_i(t)$ is the head change from hydrostatic conditions. The value of S_s used in equation (7) was calculated at each time step using equations (6a,b). We summed the changes in water levels over each of the 161 vertical nodal columns (description below) in order to compute average land surface changes for the years 1993, 1997, 2007, and 2010 across the cross section. We then subtracted the average annual land surface elevation changes along each nodal column between 1993-1997 and 2007-2010.

Equations (5-7) were solved with the finite element method model *RIFT2D* [Person and Garven, 1992]. Triangular elements that employed linear shape functions were used. *RIFT2D* was modified to account for land subsidence and uplift following Hoffman et al. [2003b]. The model domain was discretized using 13,041 nodes and 25,600 triangular elements. We developed a structured numerical grid consisting of 161 nodal columns and 81 nodal rows. In our structured mesh, vertical nodal columns are comprised of a series of nodes that have the same x coordinate but different z coordinates. This facilitates the calculation of vertical land subsidence. Nodal spacing along each column was variable. The triangular elements had an average characteristic length and height of about 40 m and 8 m in the x- and z-directions, respectively. We used a (monthly) time step of 0.0833 years over the 29 year simulation between 1982 and 2011. We included four hydrostratigraphic units (Table 2); a silt/clay dominated confining unit, a sand unit, an alluvial fan facies, and a fault zone. The sediments were assigned a uniform permeability anisotropy of 10 (k_x/k_z). The fault zone k_z was set to be 100 times greater than k_x ($k_x/k_z = 0.01$) assuming a conduit barrier

system [Bense and Person, 2006]. The distribution of silt and sand lithofacies was estimated based on geologic data from Koning et al. [2007]. The fault zone B8F (Figure 1) was included in some models. Figures 7 and 11A are similar; Figure 7 depicts small geologic details near the monitoring wells and Figure 11A represents a simplified version of this stratigraphy extrapolated to B4.

5.4 Cross-Sectional Model Results

We present two simulations, which illustrate how fault permeability influences computed head and deformation patterns. We also present a simulation in which no fault zone is present. We varied aquifer/confining, fault zone permeability, S_{ske} , and S_{skv} as part of a sensitivity study. We adjusted these parameters until we approximately matched the uplift/subsidence data. Only a narrow range of aquifer/confining unit properties could match the InSAR deformation patterns. We found that values of S_{ske} and S_{skv} of $3.8 \times 10^{-6} \text{ m}^{-1}$ and $5.6 \times 10^{-6} \text{ m}^{-1}$ produced the best fit to the observed InSAR subsidence data. Surprisingly, this is only a 1.5 increase in S_s .

During the 1993-1997 period, wells B4 and B8 (purple and red lines, Figure 2B) had similar trends of declining water levels and this is reflected in computed drawdown patterns shown in Figures 11B, 11D, and 11F. On both sides of the fault zone, significant drawdowns occurred within the sand facies for the no fault and low-permeability fault scenarios (Figures 11D, 11F). Because of the proximity of well B8 to the permeable fault zone in Figure 11B, less computed drawdown occurred on the west side of the Buckman wellfield in the high permeability fault scenario. Less drawdown occurred within the high permeability fault zone (Figure 11B) presumably because of the connection of the fault zone to the upper water table boundary. As recovery began around 2003, heads increased within the sand horizons but drawdowns within the lower-permeability silt/clay facies remained high due to slower recovery times (Figures 11C, 11E, 11G). The fault barrier scenario (Figure 11F) showed the most dramatic head differences across the fault.

As would be expected, the high permeability scenario shows the lowest net change in land subsidence rates between 1993-1995 on the west side of the fault (compare Figure 12B to Figures 12A,C). The low permeability and no fault scenarios matched the 1993-1997 trends and magnitudes in changes in land subsidence best (dashed and solid green lines in Figure 12A, 12C). However, between 2007-2010, well B8 saw recovery while well B4 continued to decline on the east side of the fault (Figure 2B). During this time the InSAR data revealed reversals in uplift and subsidence rates across the fault zone (blue, gray dashed lines, Figure 12).

6 Discussion

6.1 InSAR Observations and Modeling

The InSAR velocity maps (Figures 3-5) present long-term averages over time periods with significant well water level changes (Figures 2, S1-2) and could hence be biased by the specific timing of SAR acquisitions and their contributions to the long term average.

However, the timing during which we observe subsidence and uplift coincide temporally very well with those of aquifer depletion and recovery as suggested by the well records. The elimination of scenes that are significantly affected by atmospheric and topographic effects, as well as the small wavelength of the observed signals and their correlation with head levels gives us confidence in our observations.

The InSAR velocities do not suggest any longer wavelength flexural response due to loading and unloading of the elastic crust as observed, for instance, in California [e.g., Amos et al., 2014; Borsa et al., 2014]. This is due to the much smaller wavelength of the load removed and hence much smaller mass changes compared to the water needs of the Central Valley in California. The manifestation of such flexure is either completely absent or remains below the noise floor of the InSAR measurements, depending on the rigidity of the crust in the region.

The 1993-2000 ERS observations (Figure 3) summarize seven years of surface manifestation of high-intensity, long-term production of the underlying aquifers (Figure 2).

Our observations are similar to observations of surface responses due to aquifer depletion elsewhere [e.g., Chen et al., 2016; Chaussard et al., 2014, 2017]. We found the signals to be robust across many interferograms in ascending and descending orbits (Table 1, Figure S3).

The 2007-2010 ALOS observation (Figure 4) of deformation with opposing polarity across a sharp linear feature (potentially B8F in Figure 1) is best reproduced without invoking the mapped normal fault required to reproduce the temperature observations. A linear feature shows up in several interferograms and is considered persistent in a region with little topography. It may be stratigraphic in origin, separating discontinuous sand lenses as illustrated on Figure 7 between SF2 and SF3. The five interferograms (Table 1) going into the stacking procedure for this time interval have been picked to minimize artifacts outside of the wellfield. We find a similarly sharp feature with only subsidence on the eastern side in the 2018 average Sentinel-1 LOS map (Figure 5B). This feature's slight offset to the east when compared to Figure 4 may be an actual shift of the motion onto a different structure or stratigraphic feature due to changes in water levels in the wells in the vicinity reflecting aquifer compartmentalization (e.g., lower water levels in B4 than B6 from 2007-2010, which are reversed in 2015-2018; Figures 2B, S1, S2), due to some distortion because of different viewing geometries, or most likely due to a combination of both.

Based on these observations we find that the modeling we have performed in Sections 5.1 and 5.2 provides a convincing mechanism of uplift due to slow, longer term, long-wavelength recovery of a confined aquifer (around B8) and simultaneous fast, focused subsidence due to head changes driven by pumping at well B4 and wells in the vicinity. The close fit of the data to the no-fault conceptual model suggests that the mapped fault is not a barrier to lateral flow between wells B4 and B8; alternatively, the fault may terminate toward the south. To fully understand the pumping induced deformation field a 3D study including all wells and structure will be necessary.

The 2018 anomalously high subsidence in the eastern portion of the wellfield (Figure 5B) is most likely due to the lack of surface water supply from the poor snow pack in all of New Mexico and southern Colorado during the 2017/18 winter. Water levels in the wells for 2018, particularly well B4, confirm this hypothesis. This is similar to observations in California in response to drought conditions [e.g., Chaussard et al., 2017].

Due to the discontinuous nature of the InSAR observations, particularly between 2011-2014/15, we cannot make any definitive statements about loss of storage in this system. It appears from our observations, however, that the period of subsidence was longer lived than the recovery; most of the latter may have been achieved by the end of 2010 if judged by the well water levels (Figure 2). Since the water levels at this time appear to be close to pre-production levels, the ALOS time frame from 2007-2010 may capture the bulk of the recovery, which – at about 20 mm/yr over 3 years – significantly lags behind the initial subsidence of 15-20 mm/yr over at least 7 years. While pre-production well water levels have been reached, the inelastic deformation during the 1990s (e.g., surface cracking) suggests that at least some irreversible compaction to clay-bearing units in the Santa Fe Group sediments has occurred during this time – representing a permanent loss of aquifer storage.

The values of specific storage that best represented uplift and subsidence in the model were on the order of 10^{-6} m^{-1} . This is in the range of lithified rocks rather than poorly consolidated sediments, which are about 2-3 orders of magnitude greater ($\sim 10^{-3} \text{ m}^{-1}$; Domenico, 1972). There was little (a factor of 1.5) difference between S_{ske} and S_{skv} . Surprisingly, the absence of a fault zone best explains the paired subsidence/uplift patterns (compare blue dashed and solids lines in Figure 12C). Because these models are cross sectional and did not include all pumping wells nor three-dimensional radial flow, the model results presented in Figures 11 and 12 must be viewed as conceptual. A perfect fit to the InSAR deformation patterns should not be expected. A three-dimensional model would better represent changes in head away from the production wells, but was beyond the scope

of this study. The cross-sectional model suggested that the differential uplift/subsidence between 2007 and 2010 is due to differences in drawdown histories between wells B4 and B8 on the eastern and western portions of the wellfield. However, a relatively permeable vertical fault zone in the vicinity of well B1 and B8 is needed to allow for deeper hydrothermal fluids to migrate towards the land surface, consistent with observed elevated geothermal gradients.

It is important to note that the cross-sectional models are idealized and focused solely on conceptually assessing the effects of drawdowns on land subsidence. Cross sectional models are poorly suited to represent radial flow to a well. We overcame this limitation, to some degree, by imposing the observed drawdown history of two of the production wells nearest to the cross section. We did not attempt to represent the regional topography-driven flow system to the Rio Grande using this cross sectional model. This would have required a much more laterally expansive cross section, perhaps five times as long. The goal of these models was solely to assess how head changes due to pumping would affect land subsidence and uplift. Furthermore, it should be noted that our models assumed purely vertical deformation. Because drawdowns across the Buckman wellfield are localized, this assumption may not be strictly valid and comparisons to the InSAR LOS observations are qualitative.

6.2 Temperature Observations and Modeling

The temperature data gathered during the SAGE geophysics program reveal the complex nature of recovery following overproduction in a municipal wellfield that is situated in the discharge zone of a basin-scale hydrologic system. Both thermal modeling results and hydraulic head information suggest a two-part thermal history for the field. First, when the BWF was in high production, a significant cone of depression formed [Shomacker and Associates, 2014, 2018], creating horizontal hydraulic gradients that drew in water from shallower aquifers, thus cooling portions of the aquifer system. Then, as production generally decreased in the BWF after 2003, the cone of depression relaxed and vertical

gradients associated with the regional scale flow system began to warm the aquifer system. The thermal models used parameters that were more or less consistent with the surface deformation cross-sectional model. The best-fit hydrothermal model permeability of about $10^{-15.1} \text{ m}^2$ is intermediate between the vertical permeability of the sand and silt units used in the cross sectional models. The presence of a fault zone locally near well B8 is consistent with the requirement for elevated heat flow beneath the Buckman wellfield. The observed and simulated curvature in the temperature profile of well SF3A is consistent with downward flow of groundwater and convective cooling during the operation of the Buckman wellfield. The lack of a good fit of computed and observed temperatures near the water table is largely due to inconsistencies between the mean annual air temperature measurements (Figure 2D) and the measured temperature profiles. This suggests that transient thermal signals associated with rising water levels and upflow in the measured boreholes are currently overwhelming any downward propagating transient signals related to rising mean annual air temperature that is currently being observed in the Santa Fe area.

7 Conclusions

The combination of repeat temperature measurements and InSAR observations in a conceptual model of fluid-flow-driven ground deformation using realistic stratigraphy reveals the complexities of the BWF and its compartmentalized aquifer system. The repeat thermal profiling data were instrumental in characterizing the fault as vertically permeable in one part of the wellfield, while the InSAR data and pumping records suggest no fault (i.e., the fault is not a barrier to lateral flow) for another part of the wellfield. However, the measured local geothermal gradients constrain small-scale stratigraphy required to reproduce the observed ground displacements with our conceptual model of the wellfield. Knowledge of permeability contrasts and small-scale stratigraphy are necessary for sustainable management of the wellfield and an improved understanding of aquifer recharge.

More broadly, our combination of InSAR time series analysis and repeat temperature measurements reveals substantial dynamics of a wellfield in response to changes in wellfield management and production that we were able to reproduce in conceptual models: early groundwater pumping caused downward flow and initial cooling within the wellfield reflected in land surface subsidence; the later temperature data suggest warming and upward flow also evidenced by the simultaneous surface deformation. When compared to the early-production subsidence, the similar uplift rates over a shorter period necessary to achieve pre-production well water levels during the wellfield recovery suggest a permanent loss of storage for the BWF.

The locally elevated geothermal gradient indicates upward movement of hydrothermal fluids from depths likely exceeding 2 km near well B8, suggesting enhanced vertical permeability by faulting [Bense et al., 2008; Morgan and Witcher, 2011]. However, the modeling of the 2007-2010 differential uplift/subsidence patterns suggests the absence of a fault zone over much of the Buckman wellfield. We hypothesize that fault zone properties across the Buckman wellfield must be spatially variable and that in the vicinity of well B8, a fault zone must be locally present allowing vertical flow, consistent with the mapped fault B8F (Figure 1). In line with our hypothesis, Fairley et al. [2003] and Bense et al. [2008] found significant lateral variability in fault zone thermal behavior. Our conceptual model reveals the substantial complexities involved in turning surface observations into meaningful models of shallow subsurface dynamics. To quantitatively understand such processes, detailed stratigraphic and structural information provide essential constraints. Thermal observations can complement broad scale surface deformation locally to assess groundwater flow directions and further constrain stratigraphy locally.

Acknowledgements

RG acknowledges funding through NASA via NIP grant 80NSSC18K0805. Funding was also supplied by a grant from NM EPSCoR (OIA-1301346) and NSF-EAR grant 1830172 to Mark Person and Shari Kelley. This research was furthermore partly funded by supporters of the SAGE program, which is a program of the National Science Foundation Research Experience for Undergraduates. Major support for the SAGE program is provided by the U.S. Department of Energy and the U.S. National Science Foundation. We thank the instructors and faculty of SAGE who helped collect and analyze this data. We especially thank George Jiracek for pointing out interesting published thermal data for SF2B. We also thank Claudia Bouchet and William Schneider of the city of Santa Fe, Jack Frost with the OSE, and Joe Beeman of the USGS who helped with permissions and access. Also thanks to Dan Koning with the NMBGMR, Bill Haneberg and the New Mexico Geologic Society for their encouragement and support. We are grateful to Editor Harihar Rajaram, Associate Editor Larry Murdoch, as well as Ryan Smith and 3 anonymous reviewers for their constructive criticism and excellent comments that significantly improved this manuscript. The SAR data can be accessed through the Alaska Satellite Facility at <https://vertex.daac.asf.alaska.edu/>.

References

- Amelung, F., D.L. Galloway J.W. Bell, H.A. Zebker, and R.J. Lacznia (1999), Sensing the ups and downs of Las Vegas: InSAR reveals structural control of land subsidence and aquifer-system deformation, *Geol.*, 27(6), 483–486.
- Amos, C. B., P. Audet, W. C. Hammond, R. Bürgmann, I. A. Johanson, and G. Blewitt (2014), Uplift and seismicity driven by groundwater depletion in central California, *Nature*, vol. 509, no. 7501, pp. 483–486.
- Anderson MP (2005) Heat as a ground water tracer, *Ground Water*, 43(6),951–968.
- Annual Water Report (2018) City of Santa Fe Water Division Annual Water Report, 16 pp.
- Attema, E.P., 1991. The active microwave instrument on-board the ERS-1 satellite. *Proceedings of the IEEE*, 79(6), pp.791-799.
- Bawden, G.W., W. Thatcher, R. S. Stein, K. W. Hudnut, and G. Peltzer (2001), Tectonic contraction across Los Angeles after removal of groundwater pumping effects, *Nature*, vol. 412, no. 6849, pp. 812–815.
- Bell, J.W., F. Amelung, A.R. Ramelli, and G. Blewitt (2002), Land subsidence in Las Vegas, Nevada, 1935–2000: New geodetic data show evolution, revised spatial patterns, and reduced rates. *Environ. & Eng. Geosci.*, 8(3), 155-174.
- Bense V. F., M. Person (2006), Faults as conduit-barrier systems to fluid flow in siliciclastic sedimentary aquifers, *Water Resources Research*, 42, W05421, doi:10.1029/2005WR004480.
- Bense, V.F., Person, M.A., Chaudhary, K., You, Y., Cremer, N. and Simon, S., 2008. Thermal anomalies indicate preferential flow along faults in unconsolidated sedimentary aquifers. *Geophysical Research Letters*, 35(24).
- Berardino P., G. Fornaro, R. Lanari, and E. Sansosti (2002), A new algorithm for surface deformation monitoring based on small baseline differential SAR interferograms,” *IEEE Trans. Geosci. Remote Sensing*, vol. 40, pp. 2375–2383.
- Borsa, A.A., D. C. Agnew, and D. R. Cayan (2014), Ongoing drought-induced uplift in the western United States, *Science*, vol. 345, no. 6204, pp. 1587–1590,.
- Bredehoeft, J.D., & I.S. Papaopulos (1965), Rates of vertical groundwater movement estimated from the Earth's thermal profile. *Wat. Resour. Res.*, 1(2), 325-328.
- Buckman Direct Diversion Project informational website. (2016) Accessed on 9/16/2016 at <http://bddproject.org/about-the-bdd/how-the-bdd-works/>
- Chaussard, E., R. Bürgmann, M. Shirzaei, E. J. Fielding, and B. Baker (2014), Predictability of hydraulic head changes and characterization of aquifer-system and fault properties from InSAR-derived ground deformation, *J. Geophys. Res. Solid Earth*, vol. 119, no. 8, pp. 6572–6590.
- Chaussard, E., P. Milillo, R. Bürgmann, D. Perissin, E. J. Fielding, and B. Baker (2017), Remote sensing of ground deformation for monitoring groundwater management practices: application to the Santa Clara Valley during the 2012-2015 California drought, *J. Geophys. Res. Solid Earth*

- Chen, C.W. and Zebker, H.A., 2000. Network approaches to two-dimensional phase unwrapping: intractability and two new algorithms. *JOSA A*, 17(3), pp.401-414.
- Chen, J., Knight, R., Zebker, H. A., & Schreüder, W. A. (2016). Confined aquifer head measurements and storage properties in the San Luis Valley, Colorado, from spaceborne InSAR observations. *Wat. Resour. Res.* 52(5), pp.3623-3636.
- Delacourt, C., Briole, P., & Achache, J. A. (1998). Tropospheric corrections of SAR interferograms with strong topography. Application to Etna. *Geophys. Res. Lett.*, 25(15), 2849-2852.
- Domenico, Patrick A. Concepts and models in groundwater hydrology. (1972), McGraw-Hill, New York.
- Fairley, J., Heffner, J. and Hinds, J., 2003. Geostatistical evaluation of permeability in an active fault zone. *Geophysical Research Letters*, 30(18).
- Farr, T.G., Rosen, P.A., Caro, E., Crippen, R., Duren, R., Hensley, S., Kobrick, M., Paller, M., Rodriguez, E., Roth, L. and Seal, D., 2007. The shuttle radar topography mission. *Reviews of geophysics*, 45(2), doi:10.1029/2005RG000183.
- Fuhrmann, T., and M.C. Garthwaite (2019), Resolving Three-Dimensional Surface Motion with InSAR: L Constraints from Multi-Geometry Data Fusion, *Remote Sensing*, vol. 11 (241), doi:10.3390/rs11030241.
- Galloway, D.L., K.W. Hudnut, S.E. Ingebritsen, S.P. Phillips, G. Peltzer, F. Rogez, and P.A. Rosen (1998), Detection of aquifer system compaction and land subsidence using interferometric synthetic aperture radar, Antelope Valley, Mojave Desert, California. *Wat. Resour. Res.*, 34(10), 2573-2585.
- Grapenthin, R., F. Sigmundsson, H. Geirsson, T. Árnadóttir, and V. Pinel (2006), Icelandic rhythmicity: Annual modulation of land elevation and plate spreading by snow load, *Geophys. Res. Lett.*, vol. 33, no. 24, p. L24305.
- Grauch, V. J. S., Phillips, J. D., Koning, D. J., Johnson, P. S., & Bankey, V. (2009). Geophysical interpretations of the southern Española basin, New Mexico, that contribute to understanding its hydrogeologic framework. US Geological Survey.
- Haneberg, W.C., (2010) Preliminary Evaluation of Española Basin Aquifer Compaction Potential. Haneberg Geoscience. Prepared for the New Mexico Office of State Engineer.
- Hart, D.L., Jr., 1989, Test wells SF1a, 1b, 1c, and SF2a, 2b, 2c, Santa Fe County, New Mexico: U.S. Geol. Sur. Open-File Rep. 89-37, 24 pp.
- Hoffmann, J., H.A. Zebker, D.L. Galloway, and F. Amelung (2001), Seasonal subsidence and rebound in Las Vegas Valley, Nevada, observed by synthetic aperture radar interferometry. *Water Resources Research*, 37(6), 1551-1566.
- Hoffmann, J., Galloway, D. L., & Zebker, H. A. (2003a), Inverse modeling of interbed storage parameters using land subsidence observations, Antelope Valley, California. *Water Resour. Res.* 39(2).
- Hoffmann, J., Stanley A. Leake, Devin L. Galloway, and Alica M. Wilson (2003b), *MODFLOW-2000 ground-water model--User guide to the subsidence and aquifer-system compaction (SUB) package*. No. USGS-03-233. Geological Survey Washington DC.

- Johnson, P. S., Koning, D. J., & Partey, F. K. (2013), Shallow groundwater geochemistry in the Española Basin, Rio Grande rift, New Mexico: Evidence for structural control of a deep thermal source. *Geological Society of America Special Papers*, 494, 261-301.
- Kelley, S., M. Folsom, S. Keller, and G. Jiracek (2016), Preliminary analysis of complex subsurface temperature variations in the Buckman well field, Santa Fe County, New Mexico. In *SEG Technical Program Expanded Abstracts 2016* (pp. 4941-4945). Society of Exploration Geophysicists, Dallas, TX.
- Koning, D.J., D. Broxton, D. Sawyer, D. Vaniman, and J. Shomaker, (2007), Surface and subsurface stratigraphy of the Santa Fe Group near White Rock and the Buckman area of the Española Basin, north-central New Mexico: *New Mex. Geol. Soc., Guidebook* 58, 209-224.
- Koning, D.J., and A.S. Read, (2010), Geologic map of the southern Española basin: New Mexico Bureau of Geol. and Min. Resour. Open-file Rep. 531, ver. 1.0, scale 1:48,000.
- Kurylyk, B.L., D.J. Irvine, and V.F. Bense (2018) Theory, tools, and multidisciplinary applications for tracing groundwater fluxes from temperature profiles, *WIREs Water*, DOI: 10.1002/wat2.1329, 1-23.
- Los Alamos National Laboratory, Environmental Programs Directorate (2012), Report for the Pilot Investigation of the Buckman Well Field Piezometers. LA-UR-12-20640. EP2012-0090.
- Manning, A. H. (2009), Ground-water temperature, noble gas, and carbon isotope data from the Española Basin, New Mexico. *U. S. Geol. Sur.*
- McAda, D.P. and M. Wasiolek, (1988), Simulation of the regional geohydrology of the Tesuque aquifer system near Santa Fe, New Mexico: *U.S. Geol. Sur. Wat.-Res. Invest. Rep.*, 87-4056, 71 pp.
- Miller, M. M., Shirzaei, M., & Argus, D. (2017). Aquifer mechanical properties and decelerated compaction in Tucson, Arizona. *Journal of Geophysical Research: Solid Earth*.
- Morgan, P. and Witcher, J.C., 2011. Geothermal Resources Along the Southern Rocky Mountains and the Rio Grande Rift. *The Mountain Geologist*, v. 48, no. 4, p. 81-94.
- Murray, K. D., and R. B. Lohman (2018), Short-lived pause in Central California subsidence after heavy winter precipitation of 2017, *Sci. Adv.*, vol. 4, no. 8, pp. 1–9.
- National Weather Service (2018), New Mexico Hydrology and Drought Review, <https://www.weather.gov/abq/climonhigh2018annual-hydrodrought>, last accessed: 2019-Sep-10.
- Pavelko, M. T. (2004), Estimates of hydraulic properties from a one-dimensional numerical model of vertical aquifer-system deformation, Lorenzi Site, Las Vegas, Nevada. US Department of the Interior, US Geological Survey.
- Person, M. and Garven, G. (1992), Hydrologic constraints on petroleum generation within continental rift basins: theory and application to the Rhine Graben (1). *AAPG Bulletin*, 76(4), pp.468-488.
- Pinel, V., F. Sigmundsson, E. Sturkell, H. Geirsson, P. Einarsson, M. T. Gudmundsson, and T. Högnadóttir (2007) Discriminating volcano deformation due to magma movements and variable surface loads: application to Katla subglacial volcano, Iceland, *Geophys. J. Int.*, vol. 169, no. 1, pp. 325–338.

- Reeves, J. A., R. Knight, H.A. Zebker, W.A. Schreüder, P. Shanker Agram, and T.R. Lauknes (2011). High quality InSAR data linked to seasonal change in hydraulic head for an agricultural area in the San Luis Valley, Colorado. *Water Resour. Res.*, 47(12).
- Reeves, J. A., R. Knight, H.A. Zebker, P.K. Kitanidis, and W.A. Schreüder (2014), Estimating temporal changes in hydraulic head using InSAR data in the San Luis Valley, Colorado. *Wat. Resour. Res.*, 50(5), 4459-4473.
- Reiter, M., C. L. Edwards, H. Hartman, and C. Weidman, Terrestrial heat flow along the Rio Grande rift, New Mexico and southern Colorado, *Geol. Soc. Am. Bull.*, 86, 811-818, 1975.
- Saar, M.O. (2011) Review: Geothermal heat as a tracer of large-scale groundwater flow and as a means to determine permeability fields, *Hydrology Journal*, 19, 31-52.
- Sandwell, D., R. Mellors, X. Tong, M. Wei, and P. Wessel (2011a), Open radar interferometry software for mapping surface deformation, *Eos Trans. AGU*, 92(28), doi:10.1029/2011EO280002.
- Sandwell, David, Mellors, Rob, Tong, Xiaopeng, Wei, Matt, & Wessel, Paul. (2011b). GMTSAR: An InSAR Processing System Based on Generic Mapping Tools. UC San Diego: Scripps Institution of Oceanography. Retrieved from: <http://escholarship.org/uc/item/8zq2c02m>
- Shimada, M., Tadono, T. and Rosenqvist, A., 2010. Advanced Land Observing Satellite (ALOS) and monitoring global environmental change. *Proceedings of the IEEE*, 98(5), pp.780-799.
- Shomaker J. and Associates (2014) Buckman Wells 10-13 (RG-20516-S-10 Through S-13) Monitoring Program Biennial Report December 2014: Report prepared for City of Santa Fe Water Division, 111 pp.
- Shomaker J. and Associates (2018) Buckman Wells 10-13 (RG-20516-S-10 Through S-13) Monitoring Program 5th Biennial Report: Report prepared for City of Santa Fe Water Division, 130 pp.
- Taniguchi, M. (1995) Analyzing long term reduction in groundwater temperature due to pumping: *Hydrological Sciences Journal*, 40 (3), 407-421.
- Thomsen, D.R. and Y. Fialko, 2004, InSAR Observed Surface Deformation at the Buckman Well Field, New Mexico. In *Amer. Geophys. Un. Fall Meeting Abstracts*, 1, 0040.
- Torres, R., Snoeij, P., Geudtner, D., Bibby, D., Davidson, M., Attema, E., Potin, P., Rommen, B., Floury, N., Brown, M. and Traver, I.N., 2012. GMES Sentinel-1 mission. *Remote Sensing of Environment*, 120, pp.9-24.
- Vesselinov, V. V., D. Katzman, and D. Broxton (2014, February). Structure of Groundwater Flow in the Espanola Basin near Rio Grande and Buckman Wellfield. In *NGWA Conference on Hydrology and Water Scarcity in the Rio Grande Basin*. Nat. Groundwat. Assoc.
- Wei, M. and Sandwell, D.T., 2010. Decorrelation of L-band and C-band interferometry over vegetated areas in California. *IEEE Transactions on Geoscience and Remote Sensing*, 48(7), pp.2942-2952.

Table 1. InSAR Observation details. Master images were chosen such that temporal decorrelation and orbit baselines are minimized. Regions chosen to determine the corrections are marked in Figures 3-5 by red lines.

Mission	Date Range	Path	Frame	Flight Direction	Supermaster Image	Used scenes	Usable Interferograms	Correction
ERS	1993/07/15-2000/10/15	227	0711	Ascending	e1_21307	6	6	-8.5 mm/yr
ERS	1993/07/02-2000/10/02	098	2889	Descending	e2_04962	15	13	-6.9 mm/yr
ALOS PALSAR	2007/06/10-2010/05/03	193	700	Ascending	207450700-H1.0	6	5	-22.8 mm/yr
Sentinel-1A	2015/11/20-2018/10/23	056	471	Descending	20170713	48 (total) 28 (2015-2017) 20 (2015-2017)	62 (total) 27 (2015-2017) 35 (2018)	-61.9 mm/yr (2015-2017) -124.2 mm/yr (2018)

Table 2. Permeability assigned to different lithofacies in cross-sectional model. Note that we assumed an anisotropy of 10 (K_x/K_z) for all units but the fault zone. For the fault zone, we used $K_x/K_z = 0.1$.

Lithology	Log ₁₀ Permeability (m ²)		
	k_x/k_z		
	1	2	3
Silt	-16/-17	-16/-17	-16/-17
Sand	-12/-13	-12/-13	-12/-13
Alluvium	-11/-12	-11/-12	-11/-12
Fault	-11/-9	absent	-18/-16
Figures	10B-C, 11A	10D-E, 11B	10F-G, 11C

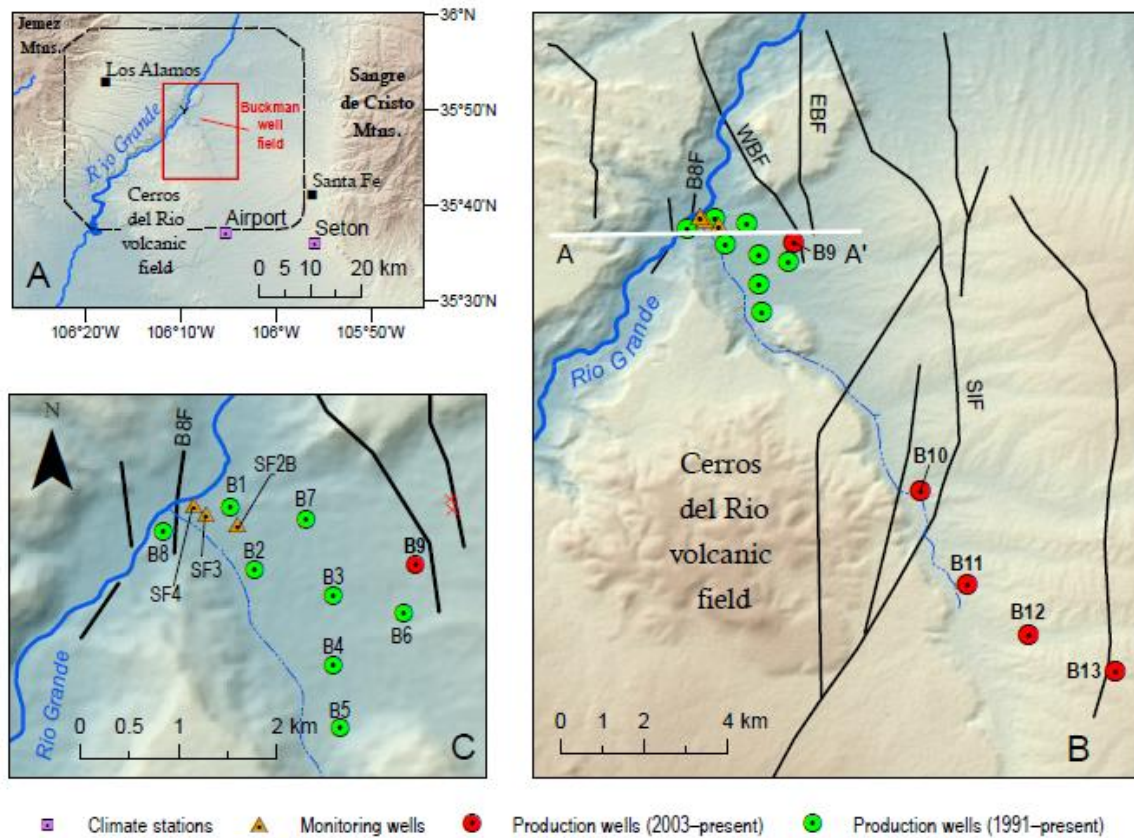


Figure 1. (A) Map showing the location the Buckman municipal well field and the climate stations used to construct Figure 2D. The dashed black line indicates the general footprint of the InSAR stacks in Figures 3-5. (B) The original wells drilled in the well field are green circles, the newer wells are red circles, and monitoring wells are orange triangles. Faults are shown as bold black lines: SIF=San Ildefonso fault; WBF=West Buckman fault; EBF=East Buckman fault; and B8F=a fault zone near well B8. Subsidence cracks formed along the East Buckman fault (red X marks the best exposures). White east-west line indicates cross-section of 2D models in Figures 10 and 11. (C) An expanded view of the original well field.

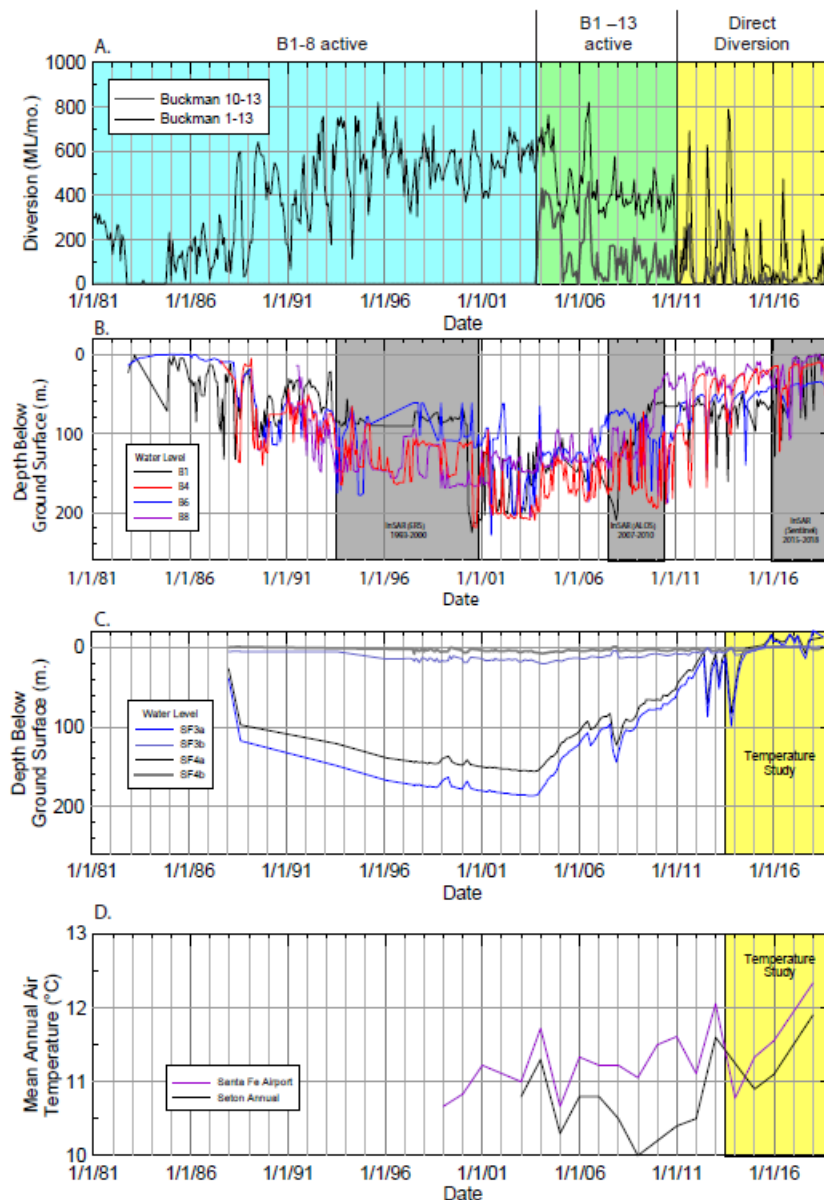


Figure 2. Buckman wellfield history. **(A)** Graph that highlights the three phases of development and water management in the field. **(B)** Water level changes in four production wells in the field and the timeframes of the InSAR analyses (See supplements for individual well records of entire wellfield). Both the production and the production well water level data were provided by the City of Santa Fe. **(C).** Water level changes in the monitoring wells and the timeframe of the repeat temperature measurements. These water level data are from the U.S. Geological Survey. **(D)** Changes in mean annual air temperature from two NOAA climate stations in the Santa Fe area.

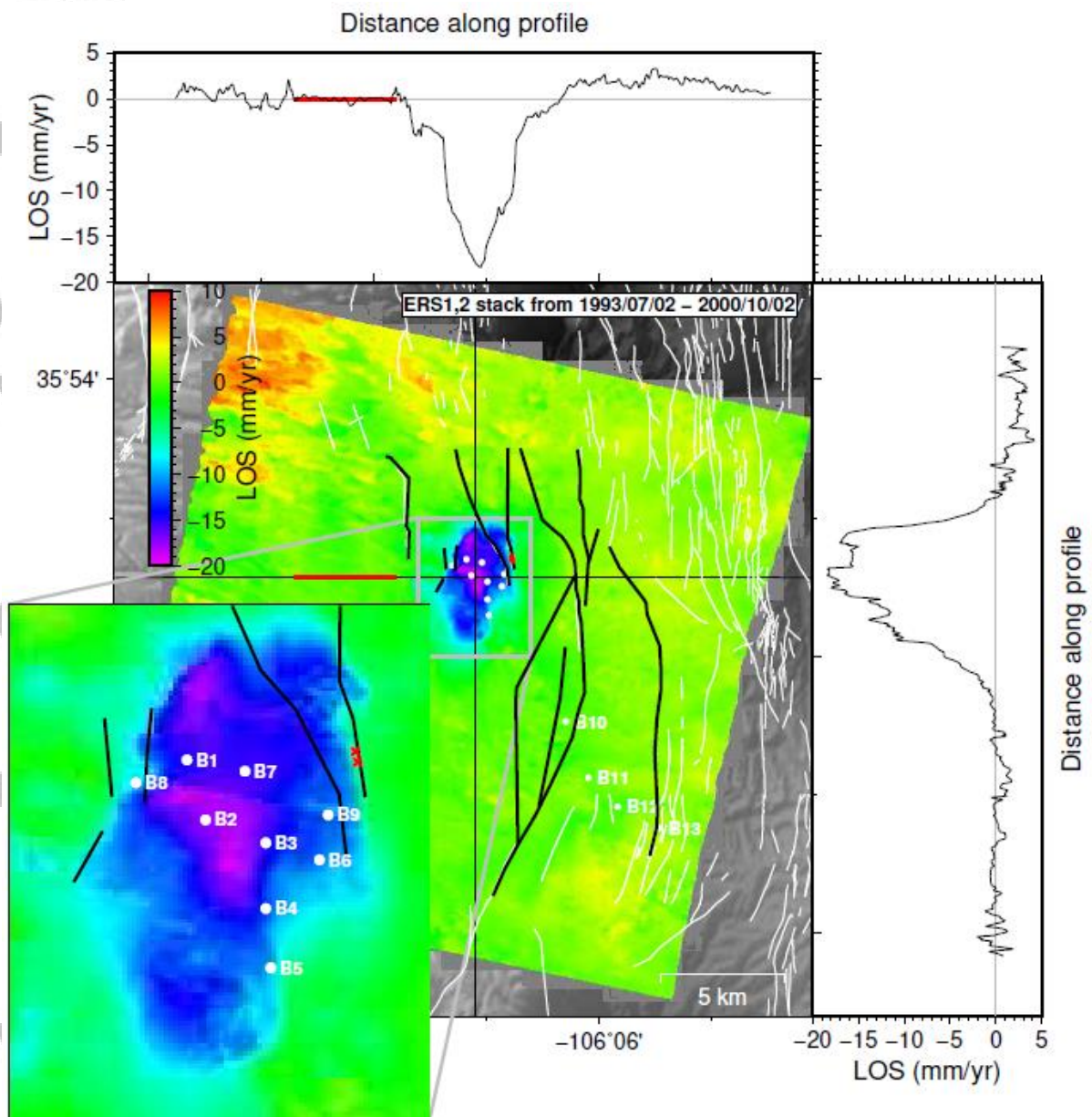


Figure 3. ERS stack showing average LOS velocity from 1993-2000 and EW (top) and NS (right) profiles through the center of subsidence. White dots are production well locations (see Figure 1), colors are line of sight velocities. Faults are marked by thick black lines (same as in Figure 1), white lines are additional regional faults. Black straight lines in main panel mark locations for EW and NS profiles of LOS velocities shown at top and right of main map (not in the same location for Figures 3-5). Red line segments in main map and top profile highlight region where velocity correction was determined (see Table 1).

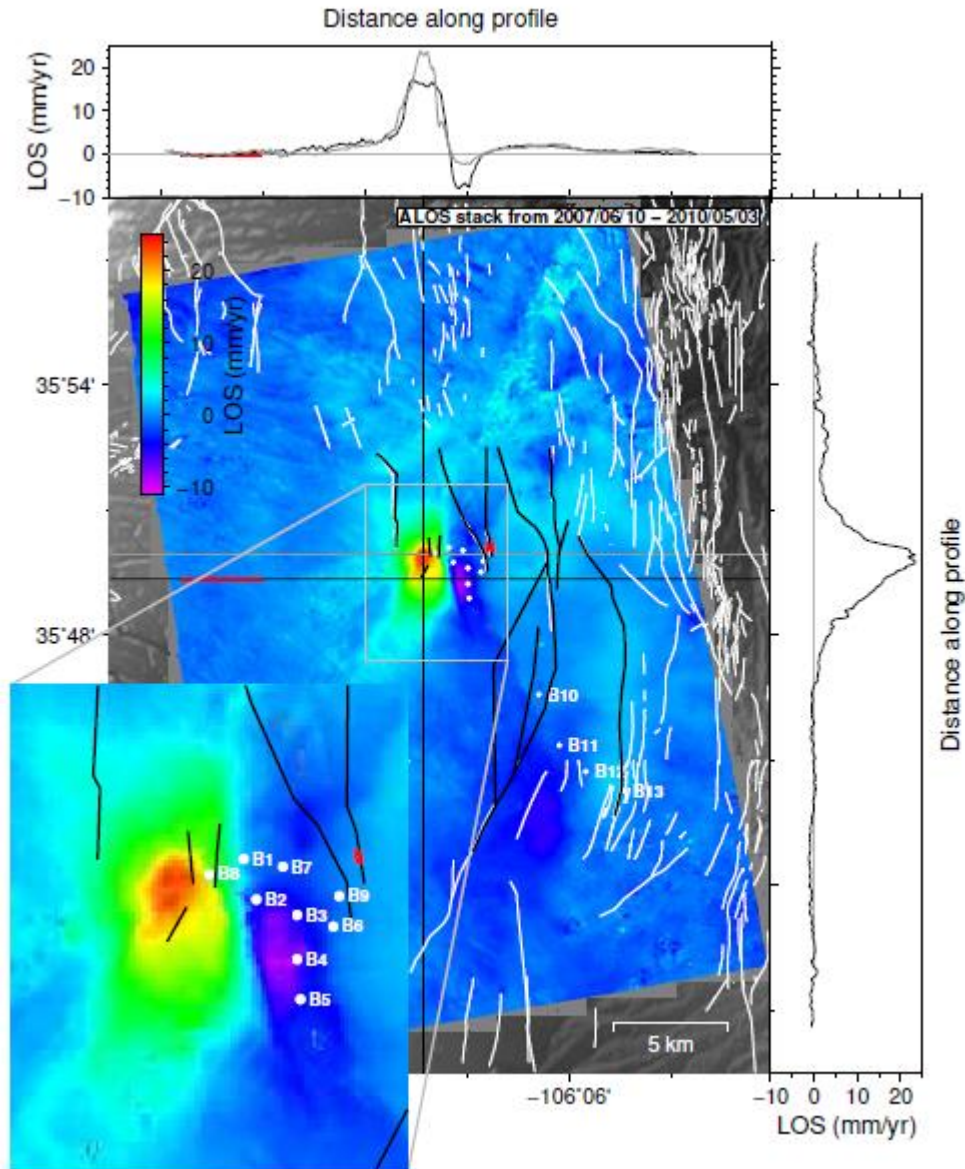


Figure 4. ALOS stack from 2007 to 2010. Similar setup to Figure 3. Note sharp discontinuity between uplift and subsidence in EW direction shown in southern EW profile (black), grey EW profile through maximum uplift feature. (Profiles are not in the same location for Figures 3-5.)

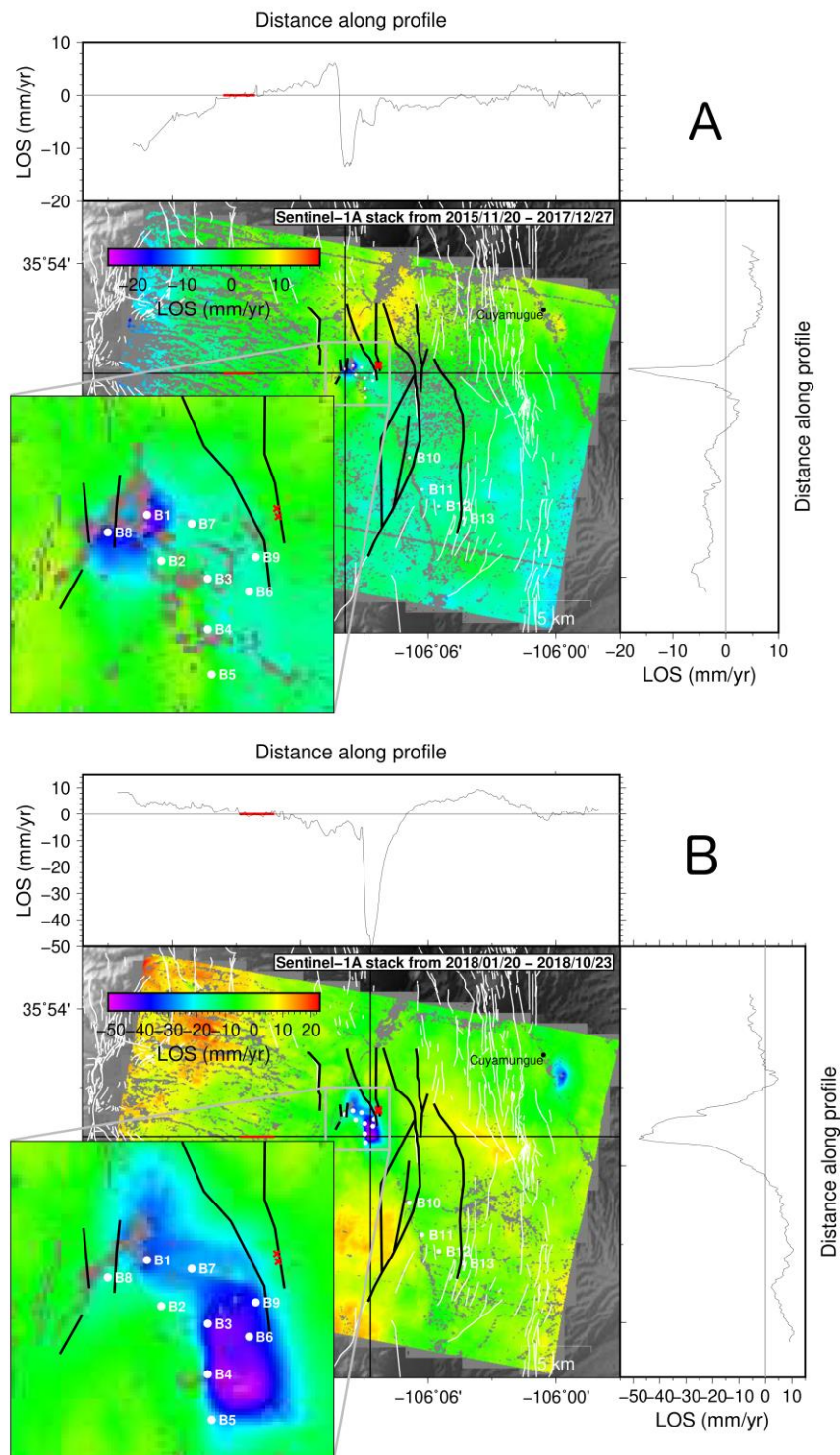


Figure 5 Sentinel-1 stack (A) 2015-2017 and (B) 2018 only. Similar setup to Figure 3. Note sharp discontinuity between east and west field in 2018. (Profiles are not in the same location for Figures 3-5.)

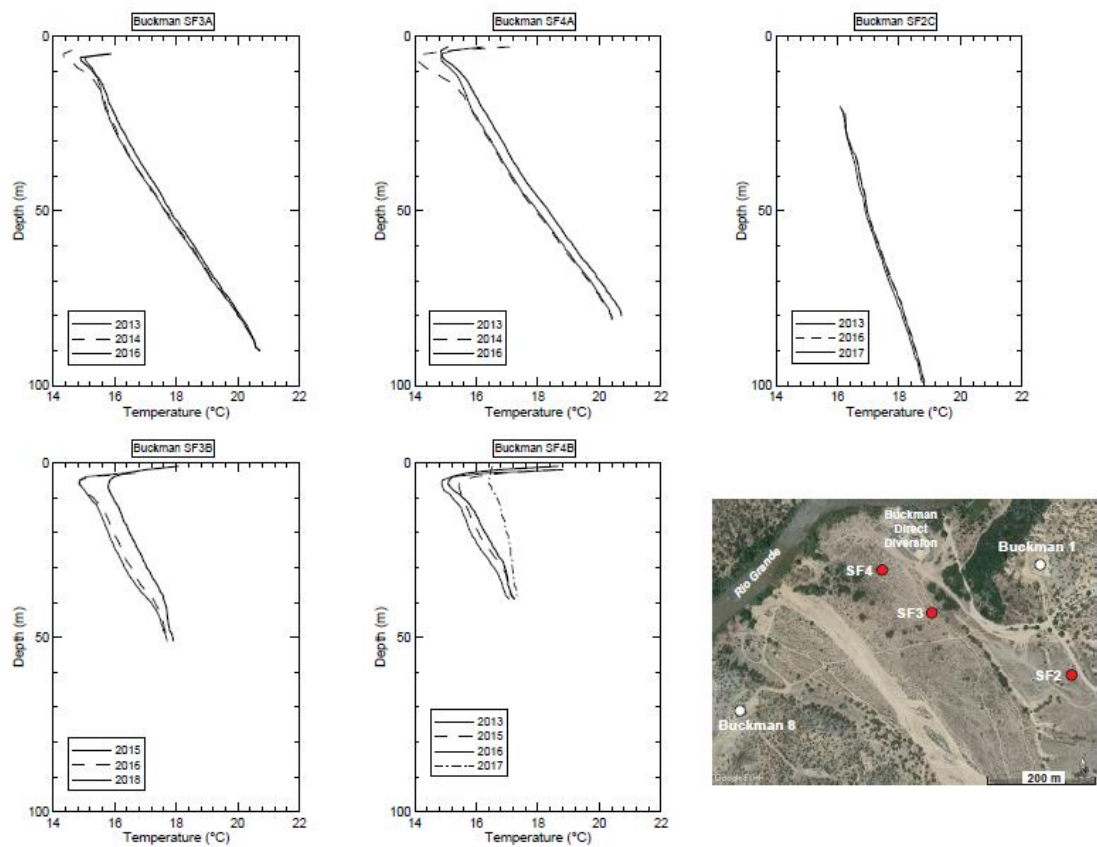


Figure 6. Thermal profiles from five monitoring wells in three piezometer nests near production wells B1 and B8. The piezometers are shown as red circles on the inset map.

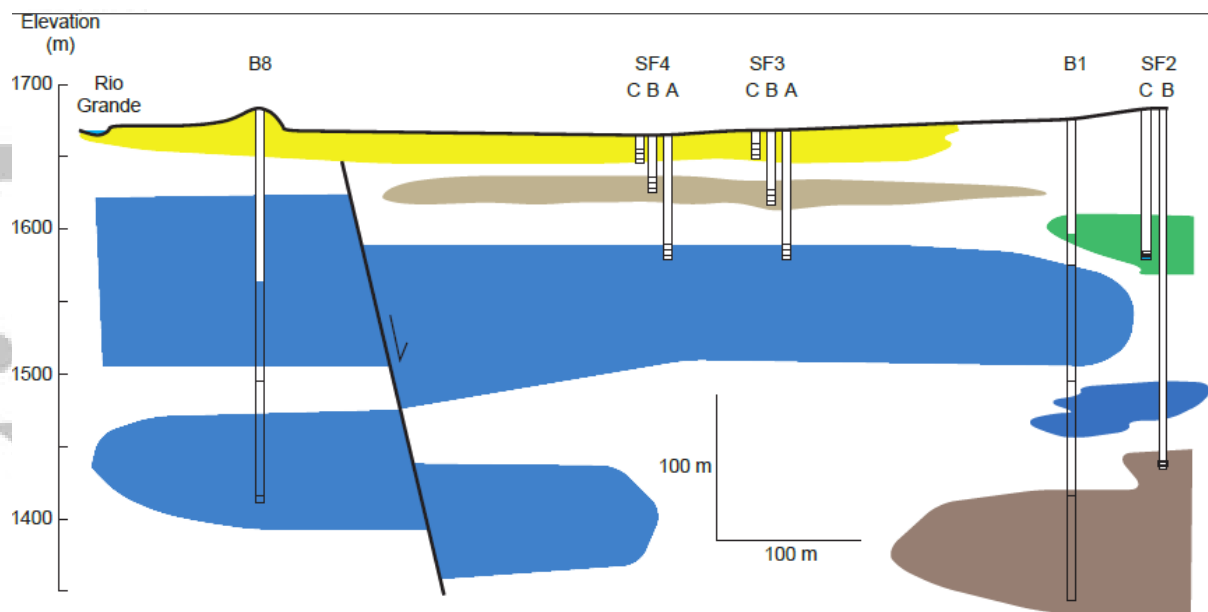


Figure 7. Conceptual cross-section through the wells illustrated in Figure 6. The screened intervals in the wells are shown as horizontal lines. Each colored layer is an aquifer and the white spaces between are confining layers. Aquifer correlations are based on interpretations of geophysical well logs, responses of water levels in the monitoring wells to pumping in the production wells, and water chemistry data. Modified from LANL [2012] and Koning et al. [2007].

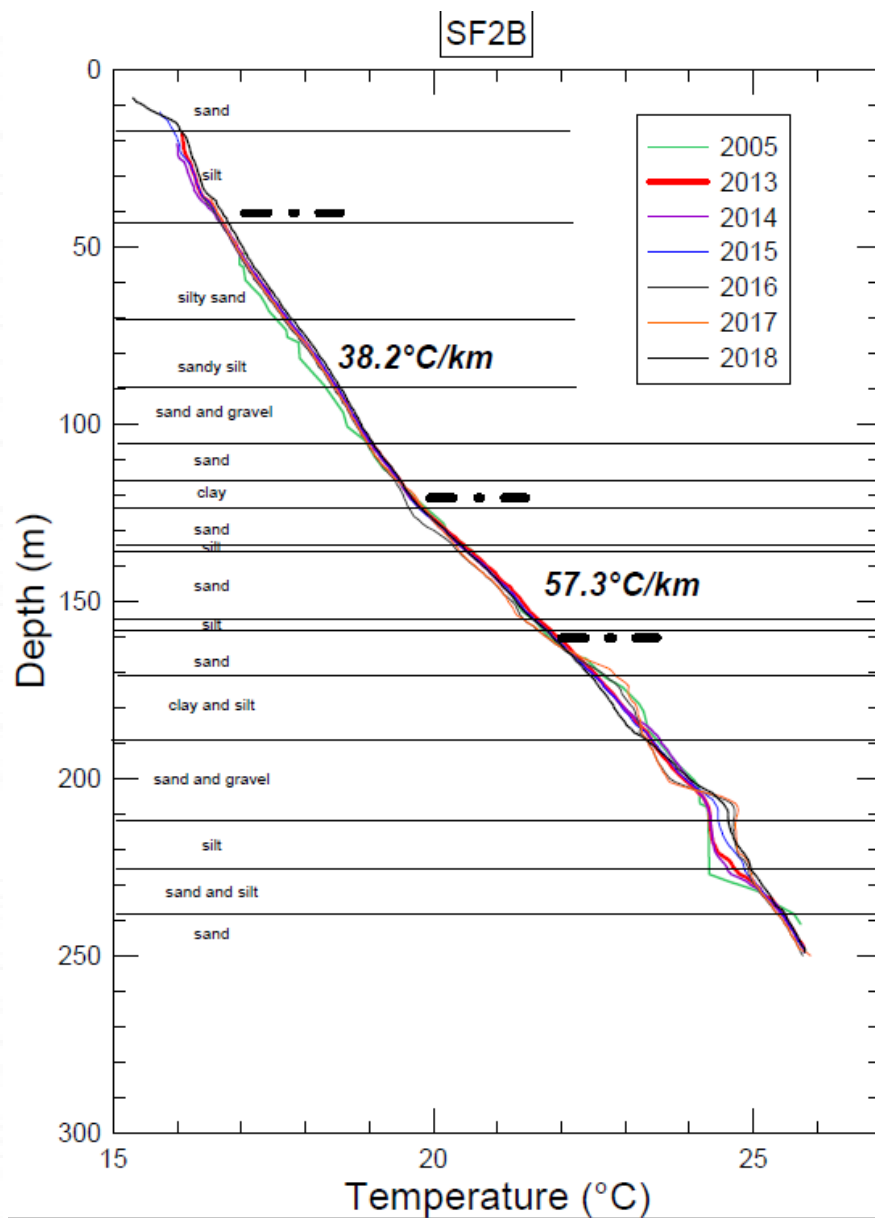


Figure 8. Thermal profiles collected between 2013 and 2018 by SAGE students from monitoring well SF2B. The 2005 log is from Manning [2009]. Lithologic information is derived from drillers log and geophysical logs for SF2A located about 3 m to the south [Hart, 1989]. The bold dot-dash lines show the top and bottom of the two gradient intervals.

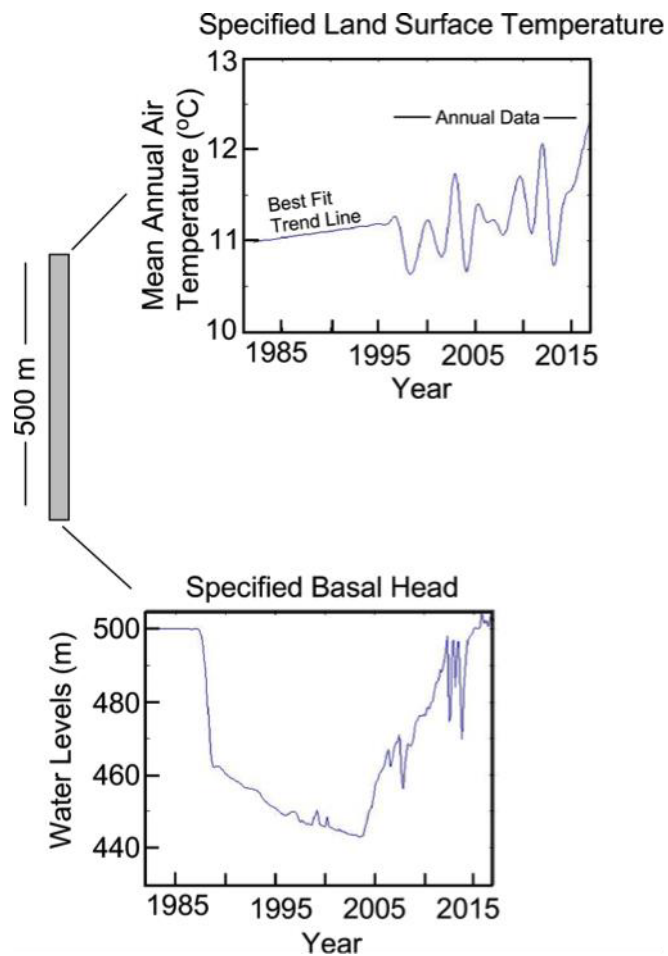


Figure 9. Hydrothermal model time dependent boundary conditions specified for at the land surface and bottom of the model domain.

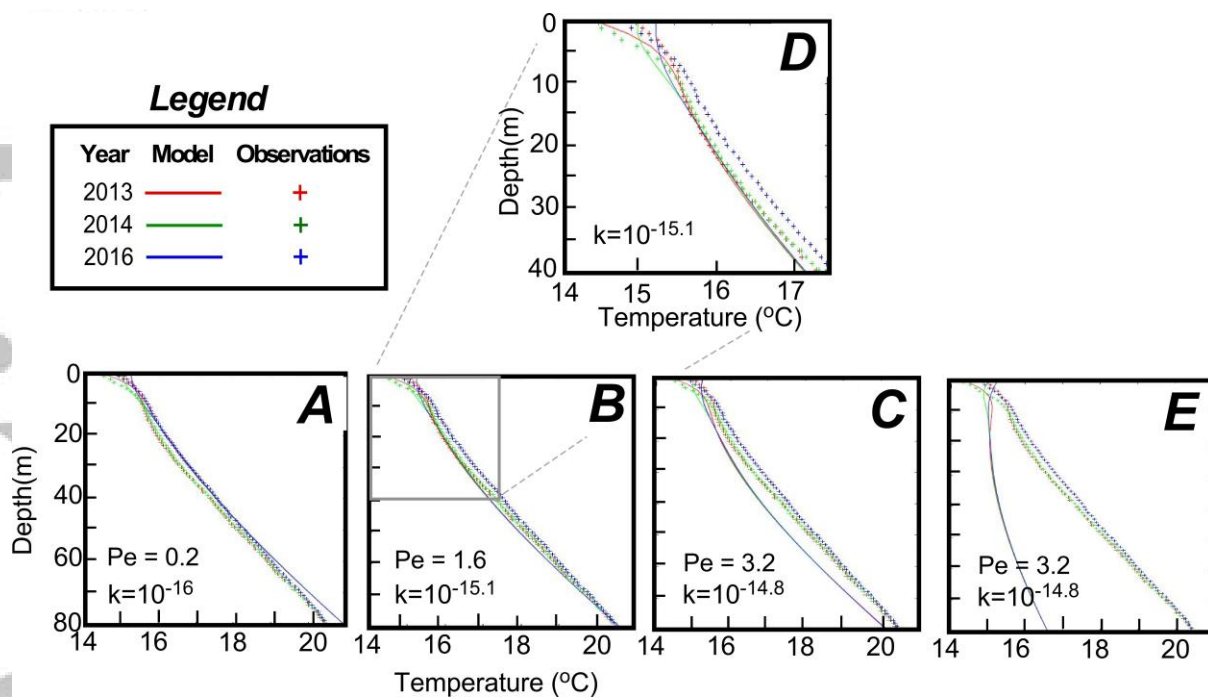


Figure 10. Effect of permeability and land surface temperature boundary conditions on simulated temperatures at Buckman well SF3A.

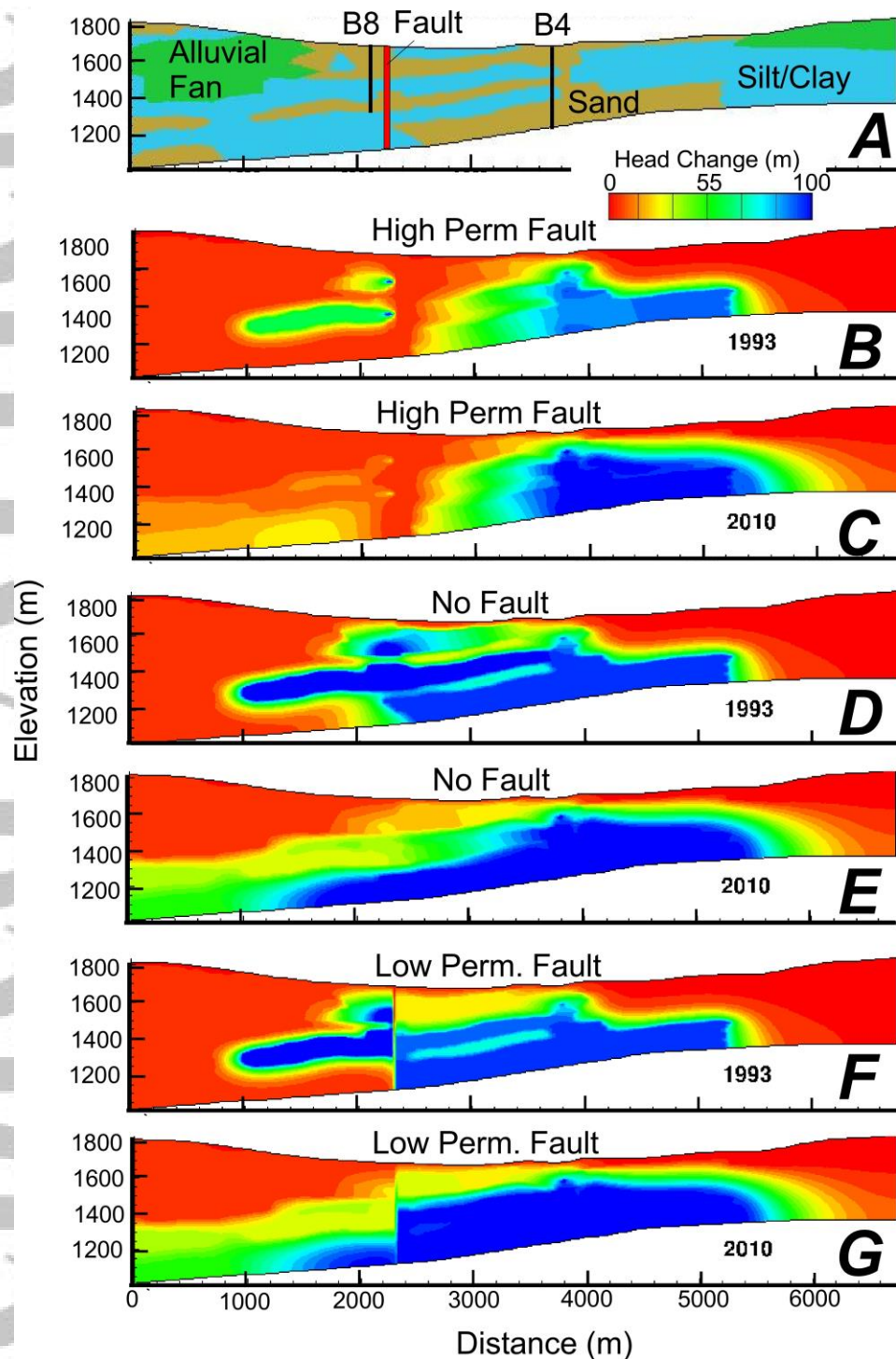


Figure 11. (A) Cross-sectional hydrostratigraphic units (green, blue, brown patterns), fault zone (red line), and locations of Buckman-8 (B8) and Buckman-4 (B4) production wells (black lines). See Figure 1B for map location of this cross-section. The permeability assigned to the 4 lithofacies/fault zones were represented in this model. (B-G) Computed 1993 and 2010 drawdown patterns for 3 different scenarios including the presence of a high permeable fault zone (B-C), no fault zone present (D-E), and a low permeability fault zone (F-G). Compressibility and specific storage decreased with depth. Observed drawdowns were imposed at nodes where the two pumping wells were located (B4, B8) is also shown in Figure 2B.

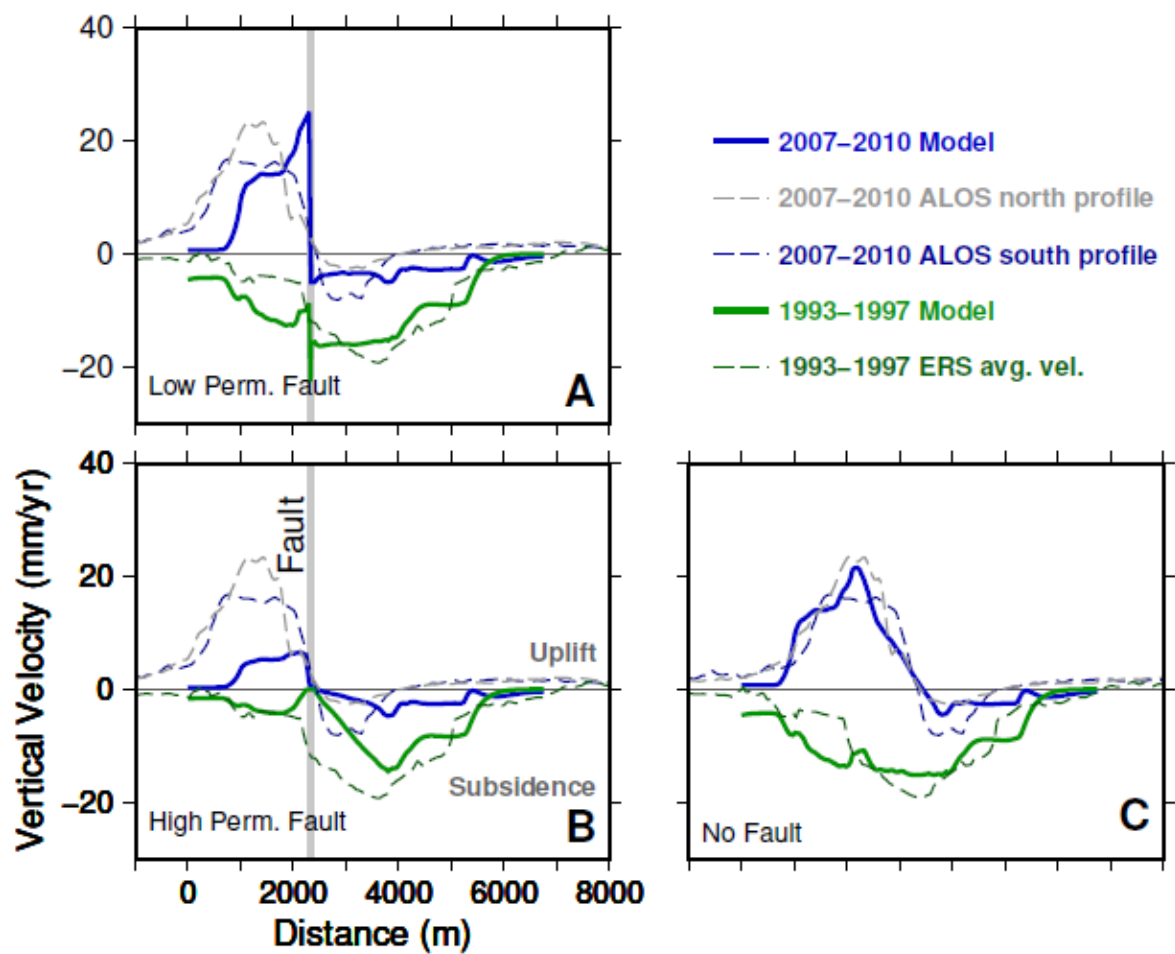


Figure 12. Observed (dashed lines, see Figures 3,4 for locations of respective EW-profiles) and calculated (solid lines) uplift and subsidence using equation a linear and non-linear elastic model (Eq. 6) for different sediment fault scenarios including **(A)** conduit-barrier fault, **(B)** high permeability fault, and **(C)** no fault present. See Figure 1B for map location of idealized cross section.